Schweizerischer Erdbebendienst
Service Sismologique Suisse
Servizio Sismico Svizzero
Swiss Seismological Service

ETH zürich

SITE CHARACTERIZATION REPORT
SCHK: Churwalden (GR), Kloster

Paolo Bergamo, Manuel Hobiger, Stefano Maranò, Donat Fäh

Last modificaction: 31.01.2018

Schweizerischer Erdbebendienst (SED)
Service Sismologique Suisse
Servizio Sismologico Svizzero
Servizi da Terratrembels Svizzer

ETH Zurich
Sonnegstrasse 5
8092 Zuerich
Schweiz
paolo.bergamo@sed.ethz.ch

Contents

Summary

The SSMNet station SCHK was installed in the village of Churwalden (GR), at the edge of a terrace on the left flank of the Churwaldnertal. The station is located next to the Church of St. Maria and Michael and the Abbot's tower, which both belong to the former abbey. In 1295, the second-largest historically reported earthquake in Switzerland occurred in Churwalden (M 6.2). This earthquake partly destroyed the church buildings at that time.

Active and passive seismic measurements were performed to characterize the subsurface structure beneath the station. The site is characterized by a relatively low fundamental frequency (0.77 Hz); at higher frequencies, a clear secondary peak at 8 Hz is found.

The subsurface structure is rather complex, characterized by a succession of river gravel layers with varying degrees of stiffness, extending down to approx. 75 m, where a weathered rock formation is met (probably limestone and slate). The morphology of the site and the reconstructed velocity models suggest that SCHK is located above a succession of river terraces.

No evidence of 2D or 3D resonance phenomena was identified, since – possibly - the terraced structure determines a seismic response closer to that of a 1D environment.

The estimated V_{S30} value for the shallower subsurface is 479 m/s, which classifies the soil as type C according to Eurocode 8 (CEN, 2004), and as type B following SIA261 (SIA, 2014). The engineering bedrock (shallowest layer with $V_S > 800$ m/s) is estimated to be located at a depth of about 23 m.

1. Introduction

In the framework of the second phase of the SSMNet (Swiss Strong Motion Network) renewal project, a new station, labelled as SCHK, was installed in near the Church of St. Maria und Michael, in the village of Churwalden (GR); the station started recording on 16th July 2015. The village of Churwalden is located in the central section of the alpine valley crossed by the river Rabiusa (Churwalndnertal), stretching approximately in a north-south direction (Fig. 1). The valley is quite narrow and incised, its bottom being circa 160 m wide at the location of the village of Churwalden. Station SCHK is located on the western side of the valley, at the edge of a gently sloping terrace, which is about 180 m wide. The center of the Rabiusa valley at Churwalden is covered by quaternary river gravel, overlying limestones, partly marls in the north-west side of the village (where SCHK is located) and marly shales, calcareous phyllite in the south-east portion (Swisstopo, 2018). The characterization of the site was ensured by two passive array measurements (array apertures of 107.7 m and 47.4 m, respectively) and an active seismic survey (recording line 22.5 m long), all carried out in close proximity with SCHK.

2. Geological setting

The valley of the Rabiusa is a typical alpine valley, deeply incised; it stretches approximately along a north-south axis for circa 15 km, opening up to the valley of the Plessur at its north end. The bottom and the lower sides of the valley are formed by moraine or formations related to fluvial or gravitative pedogenic processes: slope debris, slide deposits, rock avalanche deposits, and river gravel (at the location of the village of Churwalden). Rock outcrops are also present, belonging to the underlying formations of limestones and marly shales (Figure 1b; Swisstopo, 2018).

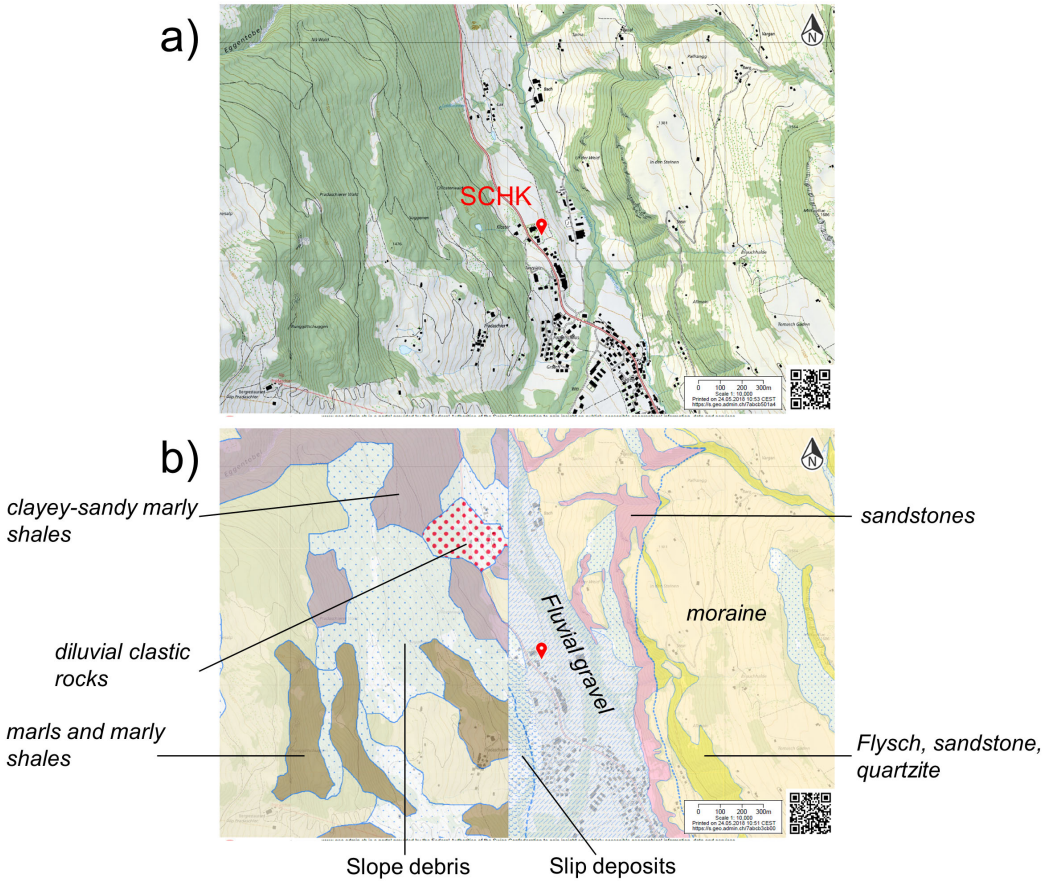

Figure 1 – a) geographical position of SCHK and b) on the Swisstopo GeoCover layer. (© 2018 Swisstopo, JD100042). The color code is the following; purple: clayey-sandy marly shales; brown: marls and marly shales; light yellow: moraine; dark yellow: flysch sandstone, quartzite; pink: sandstones; straight dashed light blue: fluvial gravel; dotted light blue: slope debris; light blue with red dots: diluvial clastic rocks; round dashed light blue: slip deposits.

3. Historical seismicity and site selection

In 1295, the second-largest earthquake that occurred in historic times in Switzerland happened in the area of Churwalden.

According to several sources this earthquake produced large damages in Churwalden. Schwarz-Zanetti (2008) gives the following two citations:

1. "Eodem anno (1295) in octava sancti Augustini per terre motum claustrum ordinis Premonstratensis Churbaldia et quindecim castra in eodem confinio funditus corruerunt." (Annales Osterhovenses [annals of the Osterhofen Abbey, close to Passau (Germany)], 1861, p. 551)[1]

[1] "In the same year (1295), the 4th of September, the monastery of the Premonstratensians in Churwalden and 15 castles in the same area have been completely destroyed by an earthquake."

2. “Terre motus in Vallesia 14 castra pro parte destruxit et crucem pinnaculi turris ecclesie maioris deiecit et in diversis locis plurima devastavit. In Curia montes scissi petre fisse sunt, plures campane pulsaverunt, quinque castra penitus destructa, plura vero fissa sunt et domus multe. Et post hunc duos alios (duo alii) motus una septimana plurimi retulerunt” (Annales Colmarienses, 1861, p. 221) [2]

The exact location of the epicenter of the earthquake cannot be found with precision, also because these reports come from faraway places. The damage corresponds to a macroseismic intensity of VIII. The Swiss Seismological Service attributes a magnitude of 6.2 to this earthquake (http://www.seismo.ethz.ch/en/knowledge/earthquake-country-switzerland/historical-earthquakes/the-ten-strongest/, last accessed January 8th, 2019), making this the second-largest historical earthquake in Switzerland.

Even if the exact epicenter of the historical earthquake cannot be determined any more, the earthquake makes the site very interesting for the installation of a strong-motion station, if possible as close to the building with the reported damages as possible. A church of St. Mary is first reported in 1149 (Bergmann, 1997). The first written records of a monastery in Churwalden are from the time between 1191 and 1196 (Bergmann, 1997). A nunnery is reported between 1208 and 1311 (Bergmann, 1997). Therefore, at the time of the 1295 earthquake, at least two churches existed in Churwalden. A painting from 1795 (Fig. 2), i.e. 500 years after the earthquake, shows the current church together with the ruins of two other churches, whose names are given as the churches of St. Niclas and St. Wolfgang in the painting. Remainings of one of these other churches were found in 1976 in a today not-existing house at Tanzplatz 41 (Bergmann, 1997). This location is slightly south of the Grischuna meat factory, the large black building indicated about 300 m south of the current church in Fig. 1.

The tower of the current church was built between 1250 and 1350 (Bergmann, 1997). As it doesn’t show earthquake damages from 1295, we assume that it was built after the earthquake. The church was largely destroyed by a fire in 1472 and renovated afterwards. Today, it is difficult to determine with precision which clock tower was the one reported to have been destroyed in 1295 and how large the actual damages have been. In any case, earthquake damages can be assumed at all churches present in Churwalden at that time.

A special interest in a seismic station in Churwalden lies in the determination of possible site effects which might amplify seismic waves at the site and are likely to have contributed to the reported earthquake damages in 1295.

[2] „An earthquake in the Valais has partly destroyed 14 castles, and it made the pinnacle’s cross of the largest tower of the church fall down and devastated in different locations many things. In Chur, mountains were broken and rocks have been fissured, several bells started ringing, five castles have been completely destroyed, many more got fissured, as well as many houses. Afterwards, two other earthquakes have been reported within one week.”

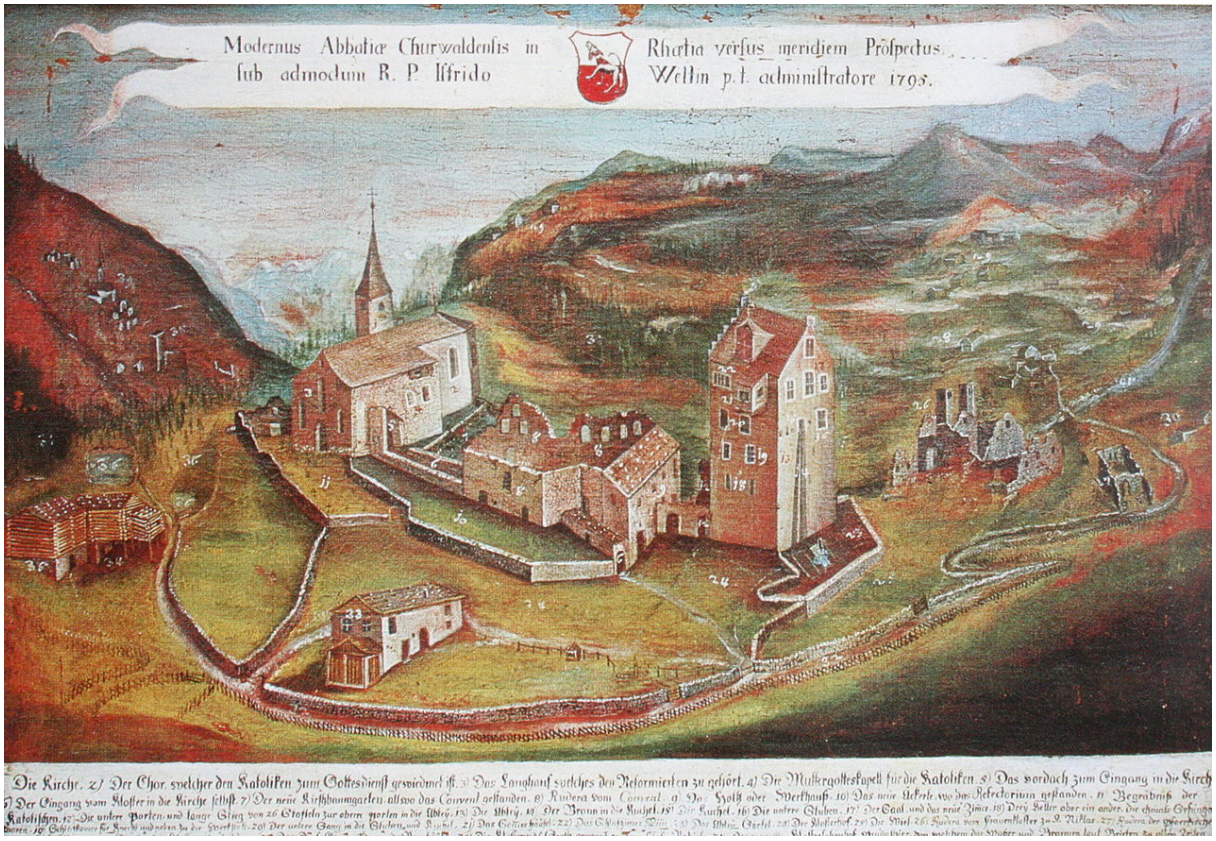

Figure 2 – Painting from 1795 showing the current church (on the left), the still existing Abbot's Tower (right) and the ruins of the churches of St. Niclas and St. Wolfgang (right).

4. Seismic acquisition

The site characterization of SCHK was carried out performing two passive array measurements and one active survey. These measurements have been performed on 24th of June 2015, i.e. before the installation of the seismic station SCHK. The locations of the measurement arrays are shown in Figure 3.

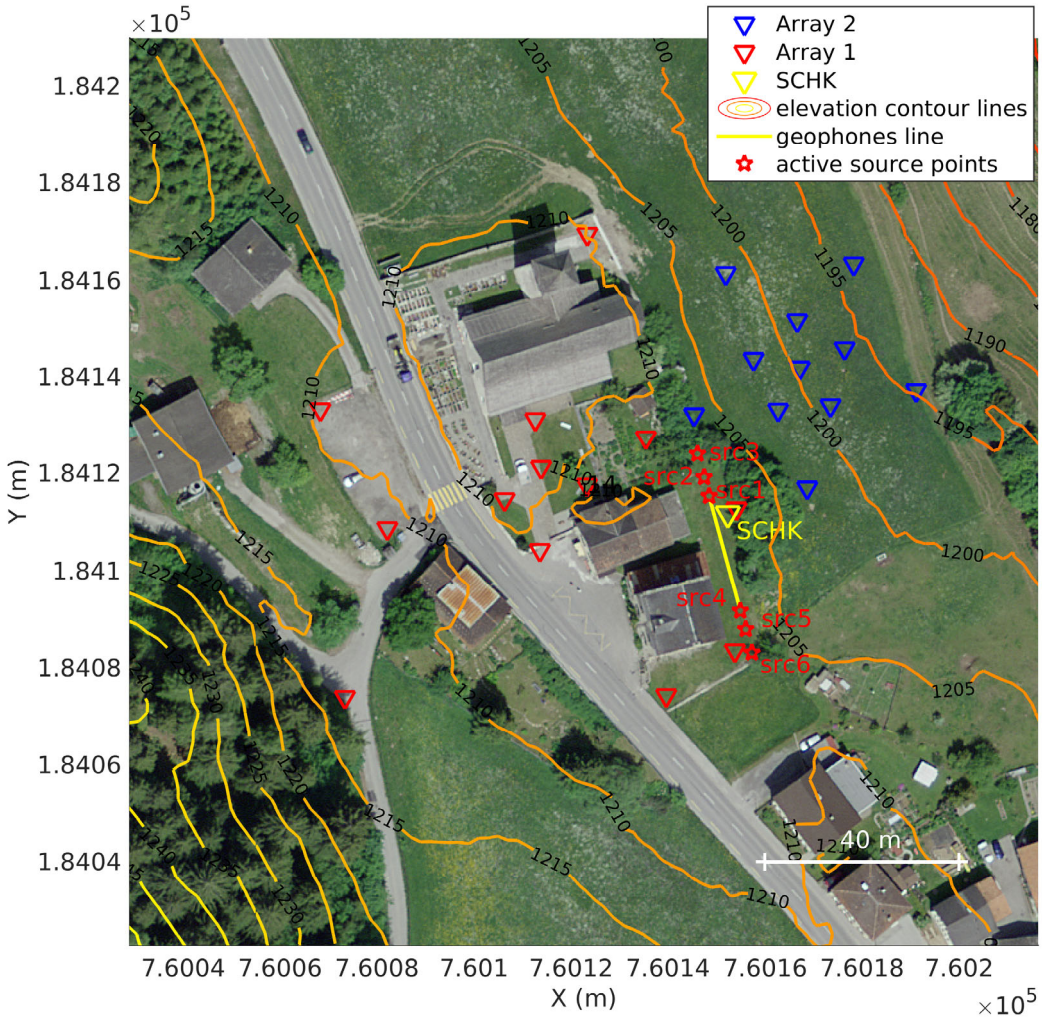

Figure 3 – Position of active and passive arrays. Red triangles: stations of passive array 1; blue triangles: passive array 2; yellow line: active survey spread; red stars: shooting points for the active survey; yellow triangle: permanent station SCHK. Contour elevation lines at 5 m intervals are also represented.

4.1 Passive seismic measurements

Array 1

The first passive seismic array was installed on the terrace around the church. It consisted of 13 seismic sensors (see Fig. 3). The layout of this array was, due to the spatial constraints, not regular.

Only in the center of the array, just to the south of the church, three stations were located on a regular circle of 10 m radius around a central station. The other stations were distributed in such a way that the array response was optimized using the available space. A fourteenth station had been installed in the northwestern corner of the cemetery, but it was not recording due to battery problems. The minimum and maximum inter-station distances in array 1 were 10.0 m and 107.7 m, respectively. The recording time was 7200 s.
The stations consisted of Lennartz 5s sensors, which had been connected to a total of 12 Quanterra Q330 digitizers (see Fig. 3). In some cases, two sensors were connected to one digitizer. The absolute times of the stations have been synchronized by GPS.
The station locations have been measured by a differential GPS system (Leica Viva GS10), which was set up to measure with a precision better than 5 cm. This precision was achieved for most stations, for the station located closest to SCHK, the measurement error was 8.9 cm, for the southwesternmost station it was 6.7 cm.

Array 2
The second passive array was installed on the slope to the northeast of station SCHK. It consisted of two concentric rings of five stations each around a central station (see Fig. 2). The radii of both rings were planned to be 10 m and 25 m, respectively, and the stations on each ring have been placed in regular angular distances. The stations on the second ring were rotated by 36° with respect to the first ring. The final array deployment resulted in minimum and maximum inter-station distances of 9.7 m and 47.4 m, respectively. The recording time of the second array was also 7200 s. The station locations have been measured in the same way as for array 1 and a precision better than 4.8 cm was achieved for all stations.

Figure 4 - Example photo of a seismic station of the passive arrays

4.2 Active survey

To ensure investigation coverage also for higher frequencies (> 10 Hz), and to investigate in detail the shallow near-surface at the location of station SCHK, an active survey was conducted in parallel with the passive recording. For the sake of a comprehensive subsurface characterization, multichannel analysis of surface waves (MASW; Park et al., 1999) and P-wave refraction (Redpath, 1973) acquisitions were conducted.

4.2.1 Equipment and geometry of the acquisition array

We used two sets of 8 three-component geophones, having a corner frequency of 4.5 Hz. Each set of sensors was connected to a Geode data logger; the two Geodes were coupled for time synchronization (Fig. 5). As a seismic source, a 5-kg sledgehammer hitting a flat metal plate was used; the synchronization between the recordings and the shooting source was ensured by a trigger device fastened to the hammer handle.
The receivers were deployed along a straight line (aligned approx. along a north-south axis) in close proximity to the final location of station SCHK. The geophones were coupled to the ground via metal spikes penetrating the soil. The inter-geophone distance was 1.5 m, leading to an array length of 22.5 m. The source was operated at six different locations, three at each end of the geophone spread (with an offset of 1, 5 and 10 m with respect to the closest receiver). The seismograms acquired with the hammer points closest to the geophone spread (offset = 1 m) were exploited for P-wave refraction analyses; traces recorded with the source positions at 5 and 10 m from the recording line were used for surface wave analysis.

Figure 5 – Active seismic array in place

4.2.2 Acquisition

The time-sampling parameters adopted for both MASW and refraction acquisitions were the following: sampling interval = 1.25 * 10^{-4} s, record length = 0.5 s, pre-trigger delay = 0 s.
The hammer blow was repeated 10 times at each shooting point; for each shot, the recordings from all geophones were saved in a separate *.sg2* file.
As example, we show the seismograms (vertical, longitudinal and transversal component) acquired with the source at the north end of the array for an offset of 1 m in Fig. 6. In the vertical component panel (left), the P-wave first break arrivals and the surface wave train are indicated with colored lines and labelled "P" and "SW", respectively.

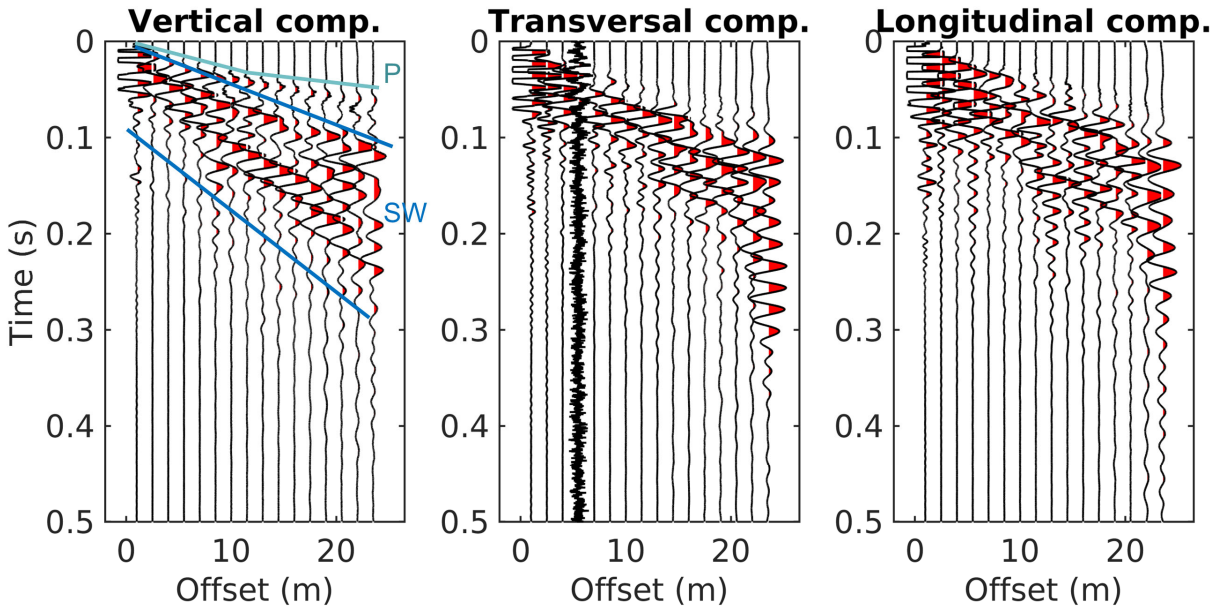

Figure 6 – Sample single-shot seismograms, with the shooting position located 1 m north of the array. In the left subpanel, the P-wave first break arrivals and the surface wave train are highlighted with colored lines and labelled "P" and "SW", respectively.

5. Data processing

Data acquired in the active and passive surveys were processed in order to determine the characteristics of propagation of surface waves (passive array acquisition) and surface and P-waves (active acquisitions).

5.1 Passive data processing

5.1.1 H/V analysis

The seismic data (three component traces) acquired by each sensor of the passive array were processed with:

- classical H/V techniques (as implemented in the Geopsy software, www.geopsy.org; classical H/V of Fäh et al., 2001), determining the spectral ratio between horizontal and vertical components, whose peaks are related to the frequencies of resonance of the site;

more refined algorithms, estimating the ellipticity of Rayleigh wave as a function of frequency (Raydec, Hobiger at al., 2009; time-frequency method, Poggi and Fäh, 2009; wavelet-based time-frequency method as implemented in the Geopsy software). These methods aim at eliminating the contributions of other waves besides Rayleigh waves, to obtain a more reliable estimation of Rayleigh wave ellipticity when compared to the classical H/V technique.

Fig. 7 collects all the H/V curves from arrays 1 and 2, obtained applying the time-frequency method of Poggi and Fäh (2010). All curves exhibit a similar appearance at frequencies below 4 Hz, with a peak identified as fundamental (f_0) in the 0.65-0.9 Hz range. The trough at 4 Hz is related with a spectral maximum on the vertical component for all stations. The horizontal components do not show a trough or peak at this frequency. Therefore, it seems that this trough is caused by a man-made source. At frequencies above 5 Hz, the H/V curves show greater variability (particularly within array 1), suggesting the presence of spatial heterogeneities in the shallower near-surface.

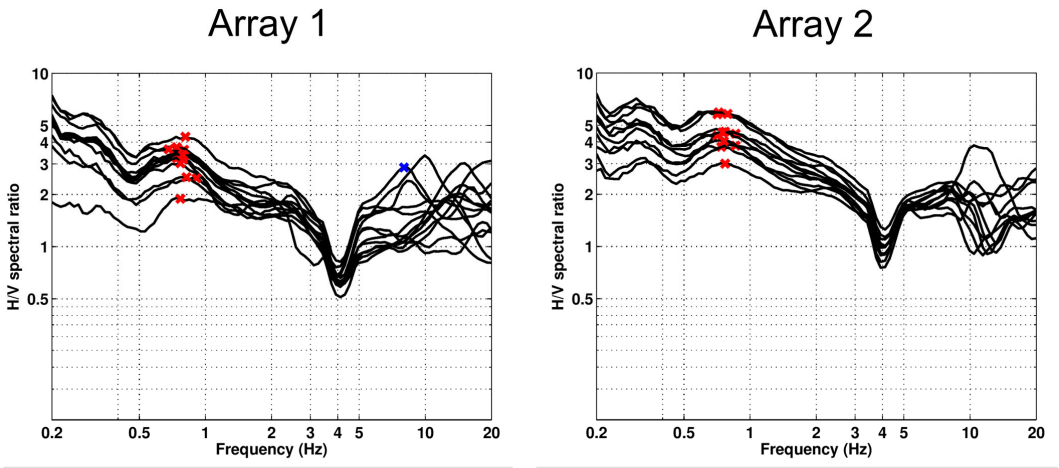

Figure 7 – H/V curves (obtained using the time-frequency method of Poggi and Fäh, 2010) from arrays 1 and 2. Red crosses mark the picked fundamental frequency; the blue cross marks a picked higher-order resonance frequency.

Fig. 8 displays some sample H/V curves. It is worth focusing on the pattern of the higher frequency (8-20 Hz) f_1 peak, which appears at most of array 1 stations (although at varying frequency abscissae), but is absent from array 2 curves (with the exception of the easternmost station; see also Figure 6).

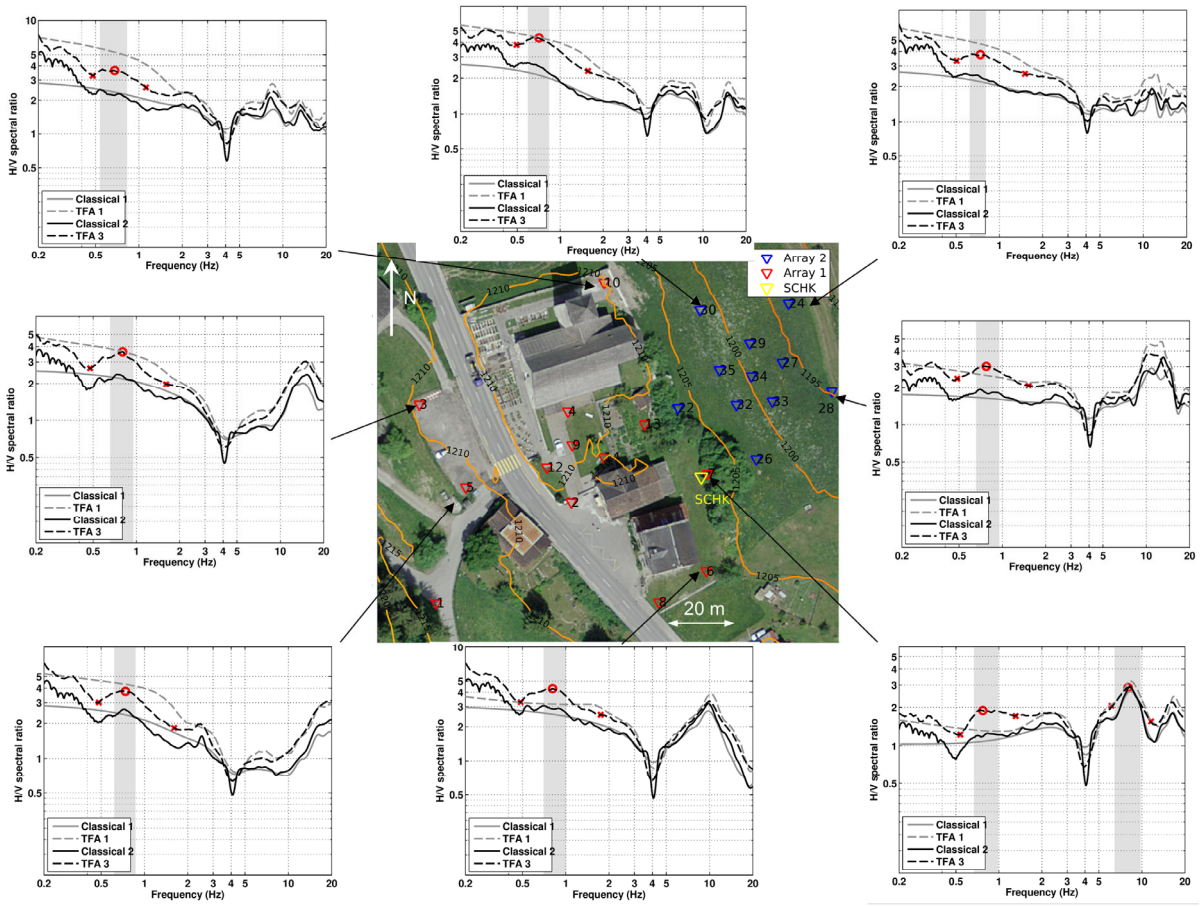

Figure 8 – H/V curves from selected passive array stations, obtained using different methods (Classical 1: Geopsy; Classical 2: Fäh et al., 2001; TFA1: wavelet-based time-frequency method as implemented in Geopsy software; TFA3: time-frequency method, Poggi and Fäh, 2010).

The main parameters of interest derived from the H/V curves, frequency f_0 and amplitude A_0 of the resonance frequency, and the higher order f_1 peak, are represented in their spatial distribution in Fig. 9. As for f_0 (whose range is anyway quite narrow), no particular spatial arrangement can be detected, suggesting that the fundamental resonance could be related either to 2D/3D resonance phenomena (Bard and Bouchon, 1985), or to an impedance contrast at depth showing little spatial variability. The corresponding amplitude values (A_0, central panel in Figure 9) seem to increase from north-east to south-west, i.e. following the terrain slope, although this trend is observed separately in the two arrays (i.e. the trend is observed among the data points from the same array, but not taking into account all H/V curves altogether). The difference between the two arrays can be due to the fact that, being deployed at different times of the days, they captured different levels of noise. Finally, the f_1 peak (mapped in Figure 9, bottom panel, array 1 only) shows a definite pattern, increasing its frequency from north-east (8 Hz) to south-west (15-20 Hz); this suggests that the f_1 peak is probably related to a sloping impedance interface below array 1 (deeper at its north-east edge, shallower at its south-west limit).

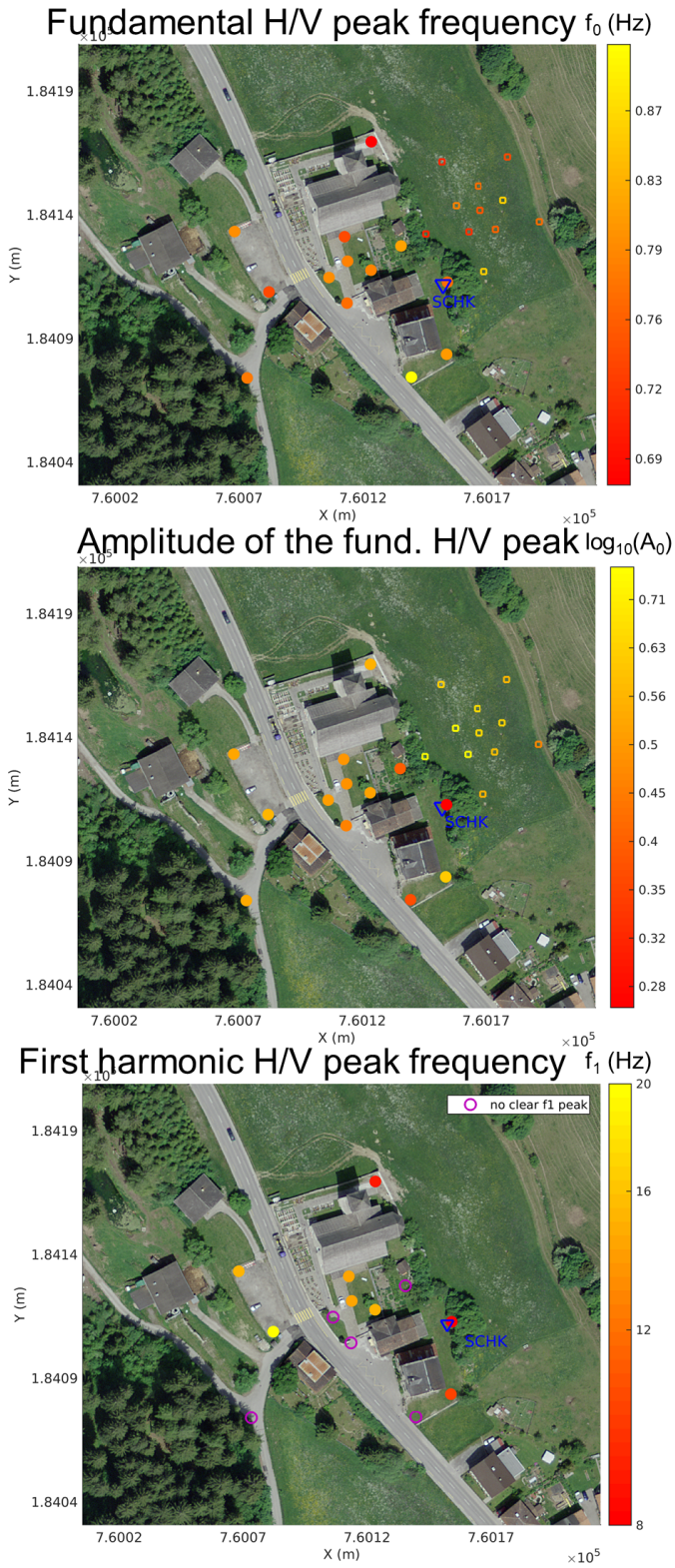

Figure 9 – Spatial distribution of the fundamental frequency f_0 (top), the corresponding amplitude A_0 (centre) and the first harmonic peak frequency f_1 (bottom, for array 1 only) from the H/V curves (obtained using the time-frequency method of Poggi and Fäh, 2010). Data from array 1 are represented with a circle, data from array 2 with a hollow square.

5.1.2 RayDec

The RayDec technique (Hobiger et al., 2009) is supposed to eliminate the contributions of other wave types than Rayleigh waves and give a better estimate of the ellipticity than the classical H/V technique. The results of this processing are shown in Fig. 10 and are similar to the H/V curves. Below 0.5 Hz, the curves are quite high and do not seem to be realistic. Between 0.5 and 3 Hz, the curves are rather flat and slightly decreasing with frequency. At 4 Hz, the artificial trough, which was also visible with the classical H/V processing, is also present. Above 5 Hz, the curves show more variability.

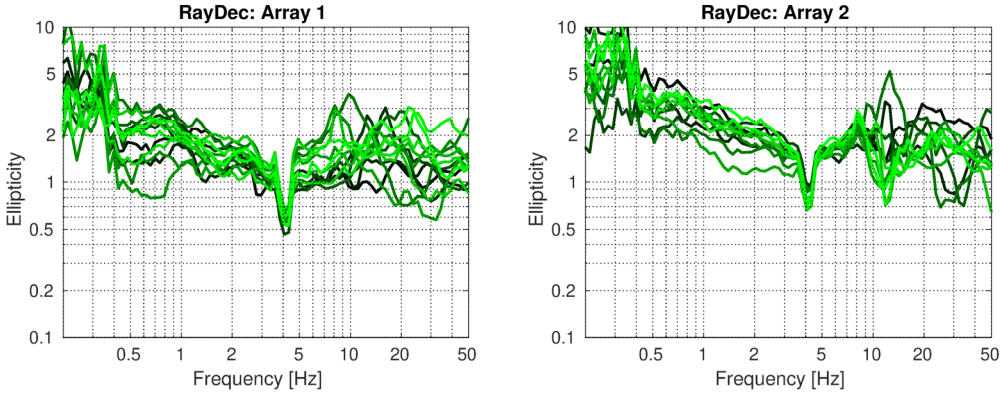

Figure 10 – Rayleigh wave ellipticity curves determined using RayDec for all stations of array 1 (left) and array 2 (right).

5.1.3 Polarization analysis

Considering the geomorphology of the site (valley flank), a polarization analysis on the array data was performed to check for 2D resonances using the method of Burjánek et al. (2012): the results are represented in Figs 11 and 12.

We remind that, according to Burjánek et al. (2012) the ellipticity is here (Fig. 11) defined as the ratio between the semi-minor and semi-major axes of the ellipse that describes the particle motion in the 3D Euclidean space for each considered time window and frequency; therefore, the particle motion related to the propagation of Rayleigh waves should be indeed characterized by low values of ellipticity, at the frequencies with prevalent horizontal motion (for which we have a peak in the H/V curves of Fig. 7). Additionally, troughs in the ellipticity graphs are also caused by 2D/3D resonance phenomena and preferential directions of noise propagation.

In our case, a match between peaks in H/V curves (Fig. 8) and troughs in ellipticity graphs (Fig. 11), can be established for the 8-20 Hz higher order peaks, but not for f_0 (0.65-0.9 Hz). This could be explained by the fact that the fundamental frequency peak does not have a sharp shape, being quite broad and without a marked amplitude increase with respect to the neighboring H/V graph (see Fig. 7).

The obtained ellipticity curves do not reach low values of ellipticity, therefore no sign of 2D or 3D resonance effects can be seen.

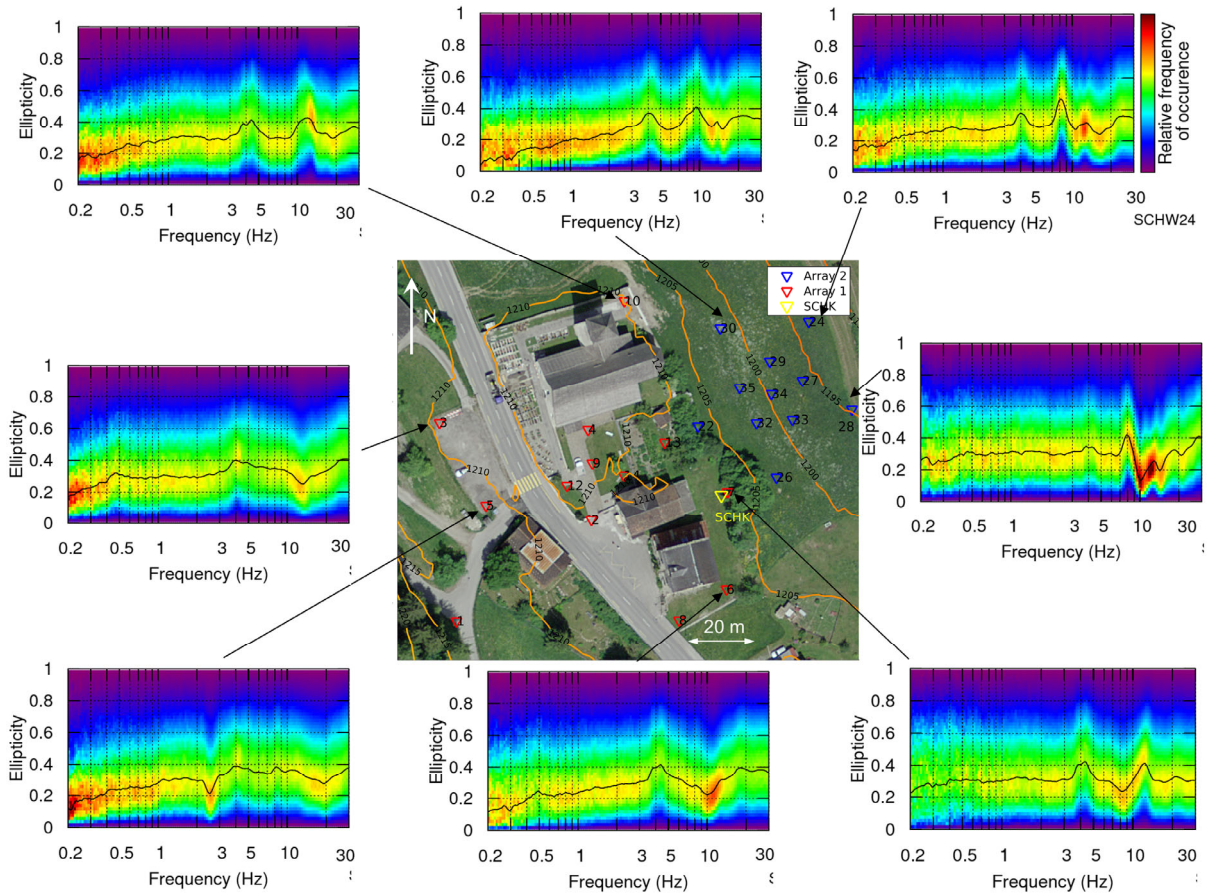

Figure 11 – Polarization analysis. The insets surrounding the map of the passive arrays contain the ellipticity (as defined in Burjánek et al., 2012) graph for some sample sensors (a trough in the ellipticity corresponds to polarized motion).

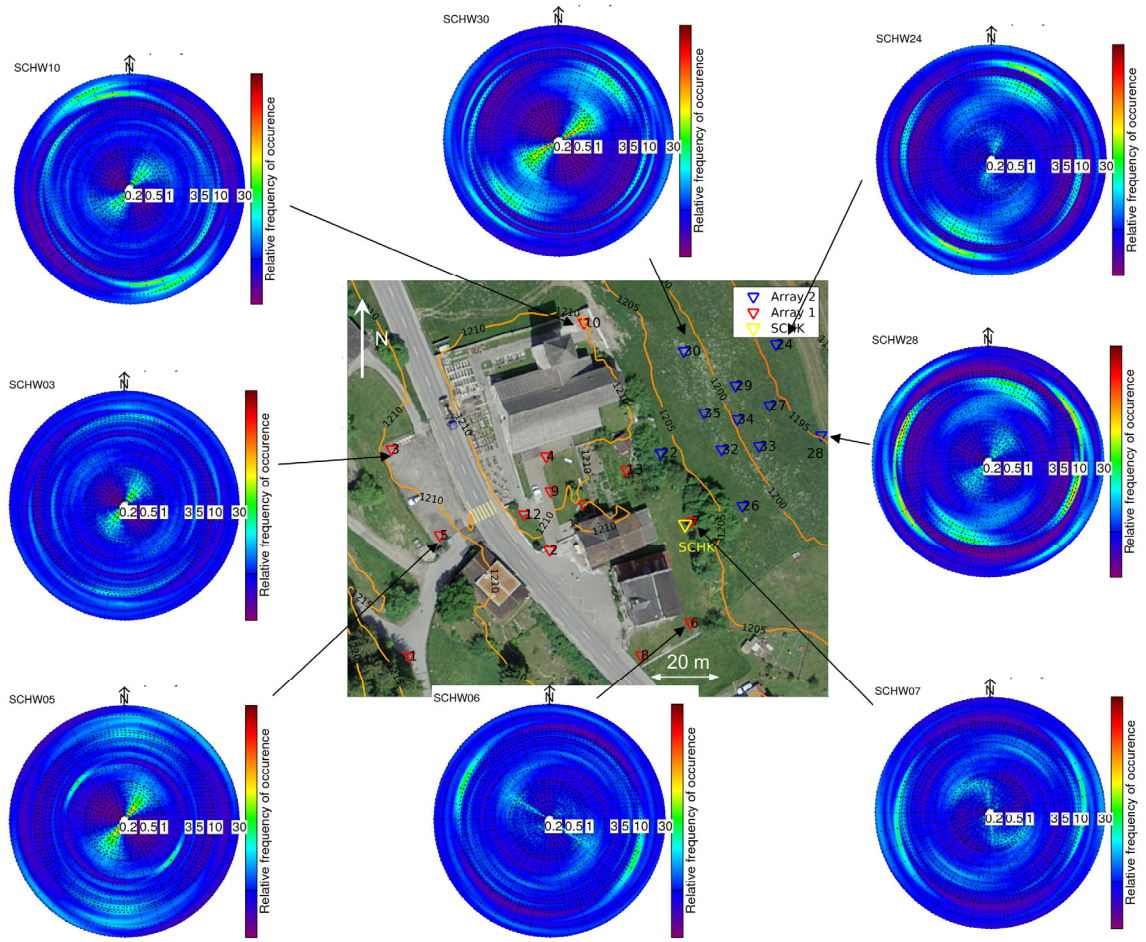

Figure 12 – Polarization analysis. The insets surrounding the map of the passive arrays contain the polarization strike graph for some sample sensors.

5.1.4 Three-component high-resolution fk

Besides single-station interpretation, the recordings from the passive array were also jointly processed with the aim of estimating the parameters of propagation (phase velocity, ellipticity, azimuth) of surface (Rayleigh and Love) waves. The used techniques are the three-component high resolution *fk* analysis (HRFK) of Poggi and Fäh (2010), and the wavefield decomposition method implemented in the WaveDec code by Maranò et al. (2012; analysis and results described in the following chapter).

The results of the high-resolution *fk* analysis are shown in Figs 13 (overall results and picking) and 17 (picked curves). As for array 1, the phase velocity dispersion curves obtained for the vertical and radial components (therefore connected with the Rayleigh wave propagation), are mutually consistent and draw a continuous branch from 5 to almost 20 Hz, with velocities gradually decreasing from 1000 m/s (at 5 Hz) to 400 m/s (20 Hz). The dispersion curve obtained for the vertical component of array 2 is in agreement with this trend, and extends the frequency range to 30

Hz with phase velocities of about 400 m/s. On the other hand, the curve for the radial component shows significantly lower phase velocities (600 to 300 m/s between 6 and 15 Hz), therefore marking a significant difference from the global pattern of the other curves. The corresponding Rayleigh wave ellipticity curves (from array 1 and 2, vertical and radial components) are rather flat and do not show marked peaks or troughs.

For Love waves, both curves for array 1 and array 2 show a quite consistent pattern in the frequency range from 5 to 10 Hz, with phase velocities decreasing from 900 to 500 m/s; the array 2 curve extends further to 14 Hz with significantly lower phase velocities of around 300 m/s. We remark the similarity between the global trend of Love curves and the radial component Rayleigh wave dispersion curve from array 2. As array 2 was located on an inclined plane and that inclination was neglected in the processing, it is possible that Love waves leaked in the radial component, thus leading to misestimating the Rayleigh wave properties on this component.

Considering the geomorphology of the site (an elongated alpine valley), prone to preferential directions of propagation, the distribution of the azimuths of the waves identified as Rayleigh and Love waves was also analyzed. The analysis was carried out on array 1 data only. Figure 14 shows that both Rayleigh (top panels) and Love waves (bottom panel) travel mostly with a north-west or south-east azimuth below 8 Hz, i.e. along the valley axis. In the intermediate frequency band from 8 to 20 Hz, waves arrive mainly from the north and east quarters and are hence presumably man-made noise sources. Vice versa, in all three plots we observe a “hole” in the south-west direction, i.e. from the mountainside (see Fig. 1).

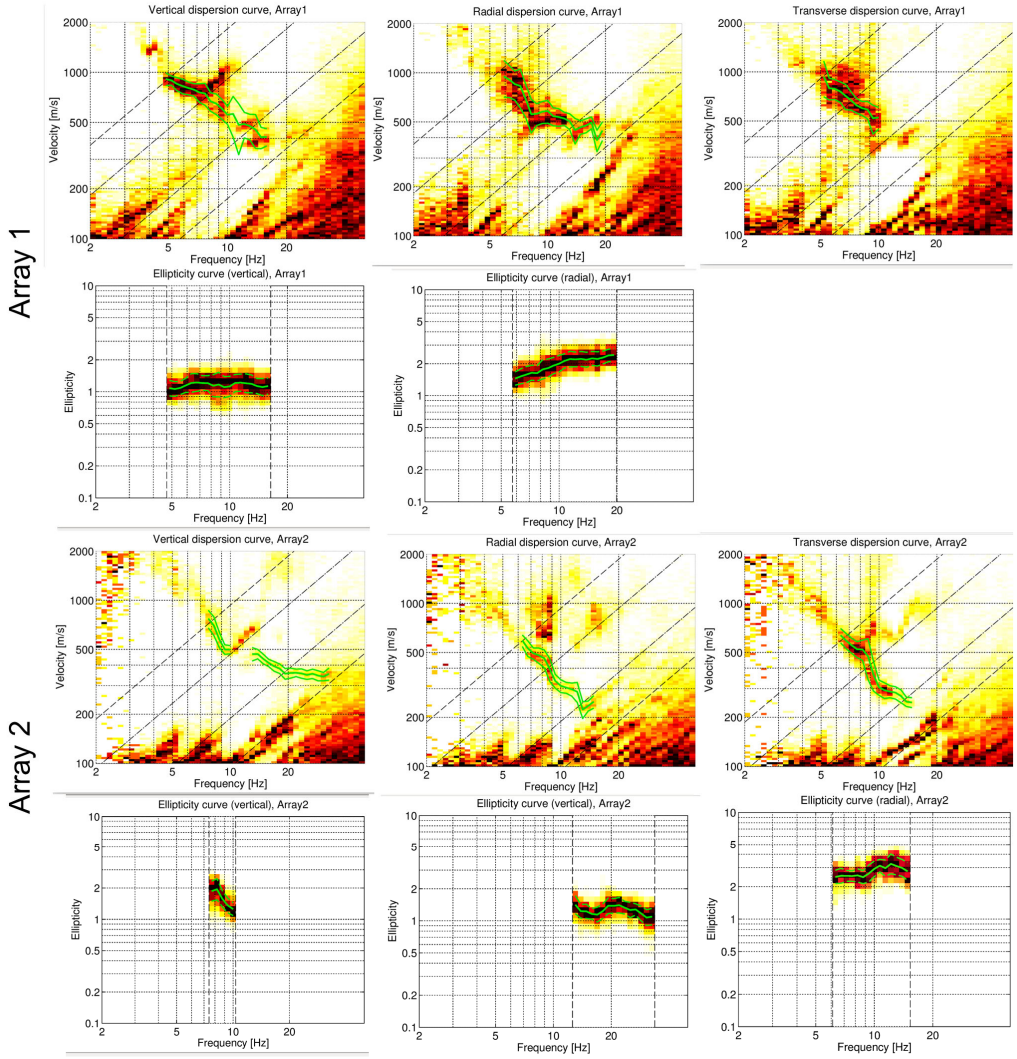

Figure 13 – Three-component high-resolution fk processing results. Phase velocity vs frequency graphs obtained from the three components from array 1 (top row) and array 2 (third row from top); ellipticity curves obtained from vertical and radial components (second row: array 1; bottom row: array 2). Dashed lines indicate the array resolution limits, while green lines indicate the picked curves (central values and standard deviation interval).

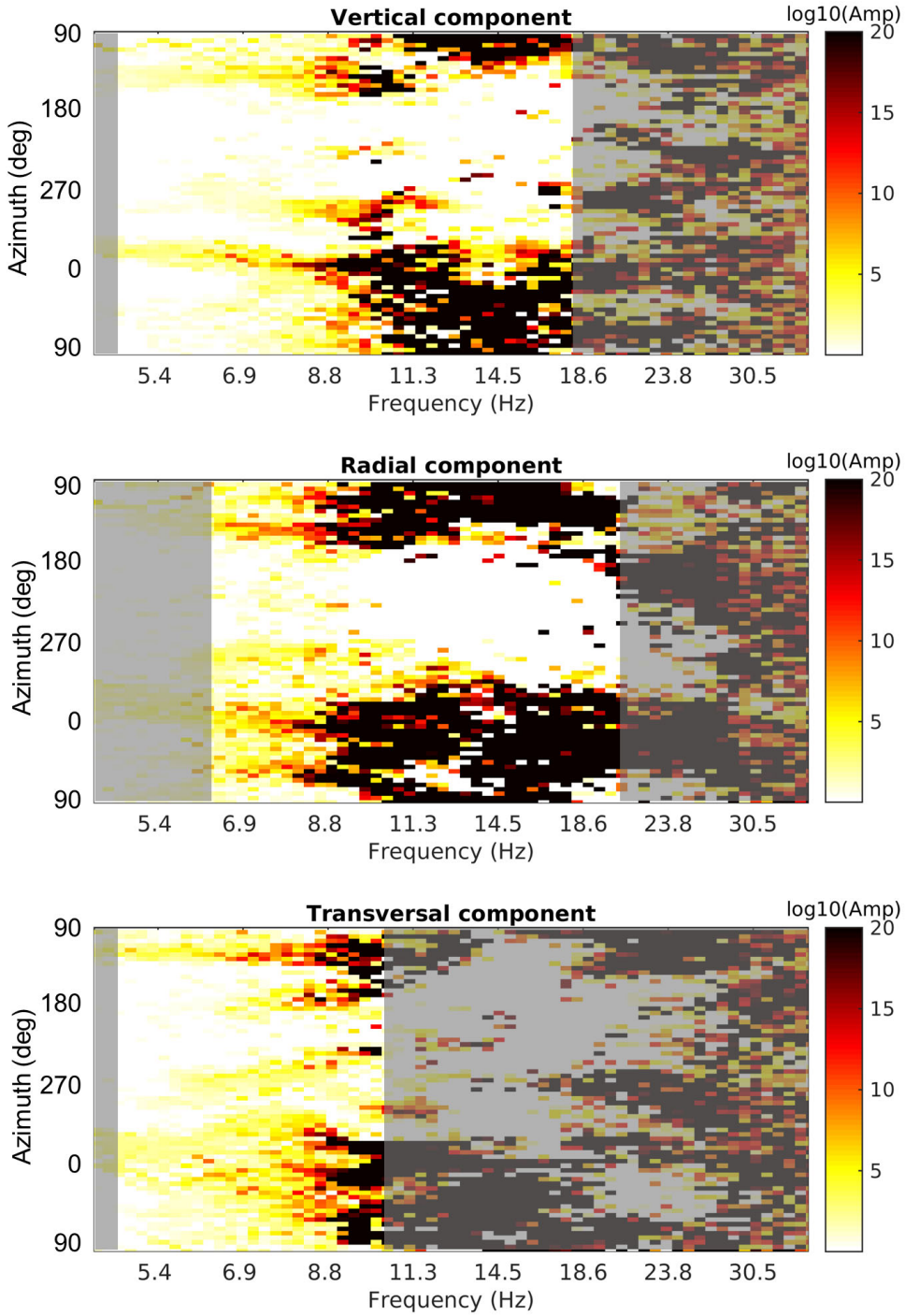

Figure 14 – 3C-HRFK, array 1. Azimuth distribution of amplitude values, as a function of frequency, for the waves appearing in the vertical (top), transversal (center) and radial (bottom) component recordings. The azimuth is measured clockwise in degrees from the north, so that 0 deg = North, 90 deg = East, 180 deg = South, 270 deg = West. Only the data with phase velocities in the range of identified Love and Rayleigh wave dispersion curves (300 – 1100 m/s) were considered for the representation; frequency bands outside the picked dispersion curve range are shaded in gray.

5.1.5 Wave field decomposition

The passive seismic data acquired by arrays 1 and 2 were also processed with the wave field decomposition technique implemented in the WaveDec code by Maranò et al. (2012). The code jointly analyzes all recordings from all sensors and components, estimating the parameters (phase velocity, ellipticity) of Rayleigh and Love wave propagation. The recorded wave field is subdivided into time windows, and each window is decomposed into a number of waves that explain it best; wave propagation parameters are then estimated for each wave with a maximum likelihood approach. The sharpness of the wave property estimation can be modified the between purely maximum likelihood estimation and a Bayesian Information Criterion by changing a parameter called γ. Here, a value of $\gamma = 0.2$ was used, corresponding to a mainly maximum likelihood estimation.

The WaveDec results are shown in Figs 15 and 16. For array 1, we can pick the Love wave dispersion curve from 4.7 to 15.1 Hz and the Rayleigh wave dispersion curve from 5.3 to 15.7 Hz. Both dispersion curves show a velocity decrease from about 1000 m/s to less than 400 m/s in that frequency range. The ellipticity angle is negative in the whole frequency range, corresponding to retrograde particle motion.

For array 2, the results are less clear (Fig. 16). The Love wave dispersion curve can still be retrieved from 6.3 to 16.9 Hz, but the Rayleigh wave dispersion curve is only visible from 6.7 to 9.4 Hz. Both curves seem to be anyhow compatible with the results from array 1.

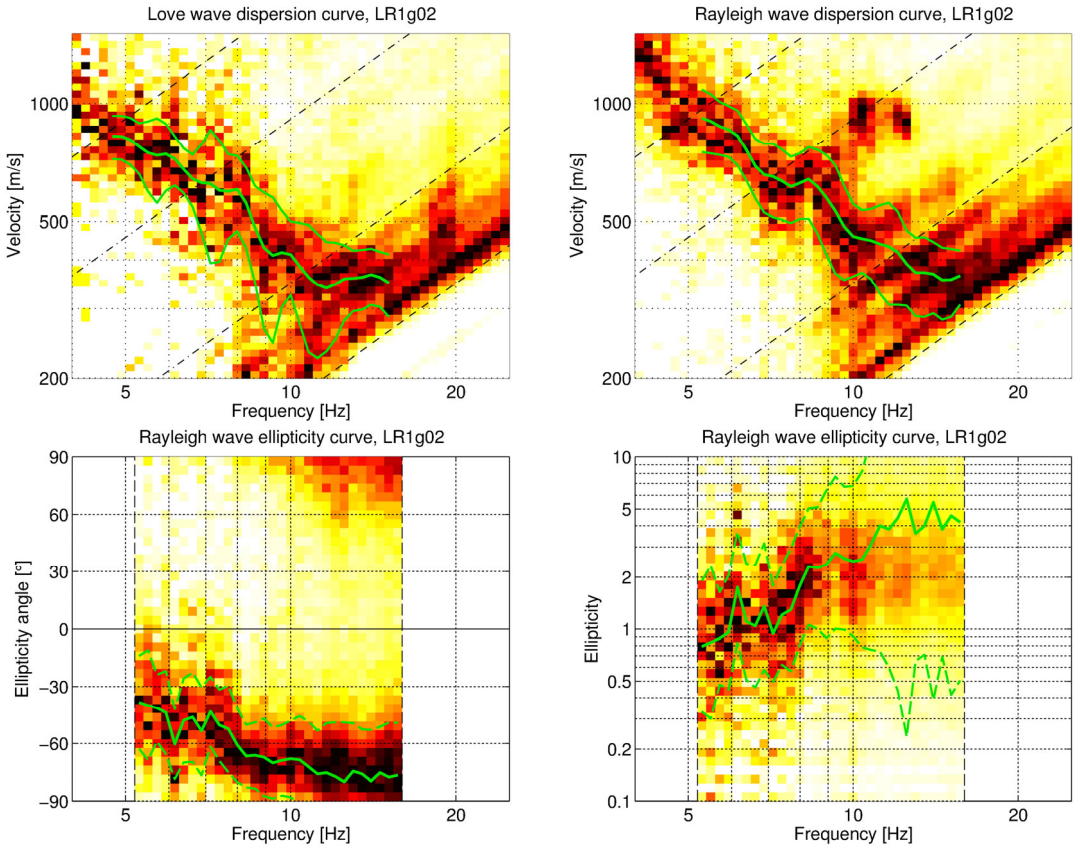

Figure 15 – Love and Rayleigh wave dispersion (top) and ellipticity (bottom) curves obtained with the WaveDec technique (Maranò et al., 2012) for array 1. The dashed lines indicate the theoretical array resolution limits, the central green line indicates the picked curves, the upper and lower green lines indicate the standard deviation.

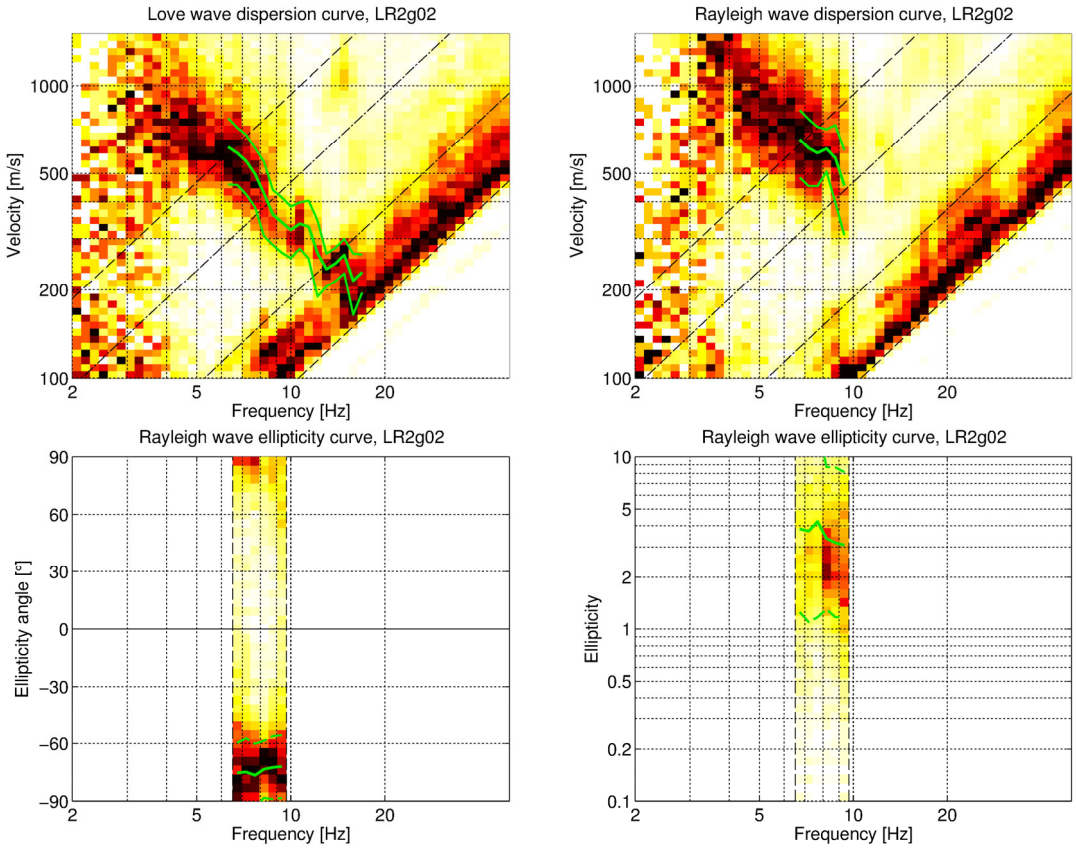

Figure 16 – Love and Rayleigh wave dispersion (top) and ellipticity (bottom) curves obtained with the WaveDec technique (Maranò et al., 2012) for array 2. The dashed lines indicate the theoretical array resolution limits, the central green line indicates the picked curves, the upper and lower green lines indicate the standard deviation.

5.1.6 Comparison of the results

The results of the different processing techniques for the passive data recordings are compared in Fig. 17. The Love wave dispersion curves of the different methods fit together quite well, with some larger differences between the WaveDec curve for array 1 at higher frequencies and the HRFK and WaveDec curves for array 2, which are slower above 10 Hz. Array 2 was located on an inclined field and might therefore have a lower wave velocity in the superficial layers than array 1, which was located on top of the terrace structure.

For Rayleigh waves, the dispersion curves of the different methods and both arrays fit together, except for the curve obtained using the radial components on array 2. This radial dispersion curve is actually very close to the Love wave dispersion curve of array 2. We therefore interpret it as a misidentified Love wave dispersion curve. The vertical dispersion curves of array 2 are in fact in rather good agreement with the dispersion curves for array 1. The Rayleigh wave ellipticities obtained with the different array methods are quite variable and only available at frequencies above 5 Hz. The RayDec ellipticity curve for the station closest to SCHK covers a wider frequency range and is very flat, except for the artificial trough at 4 Hz.

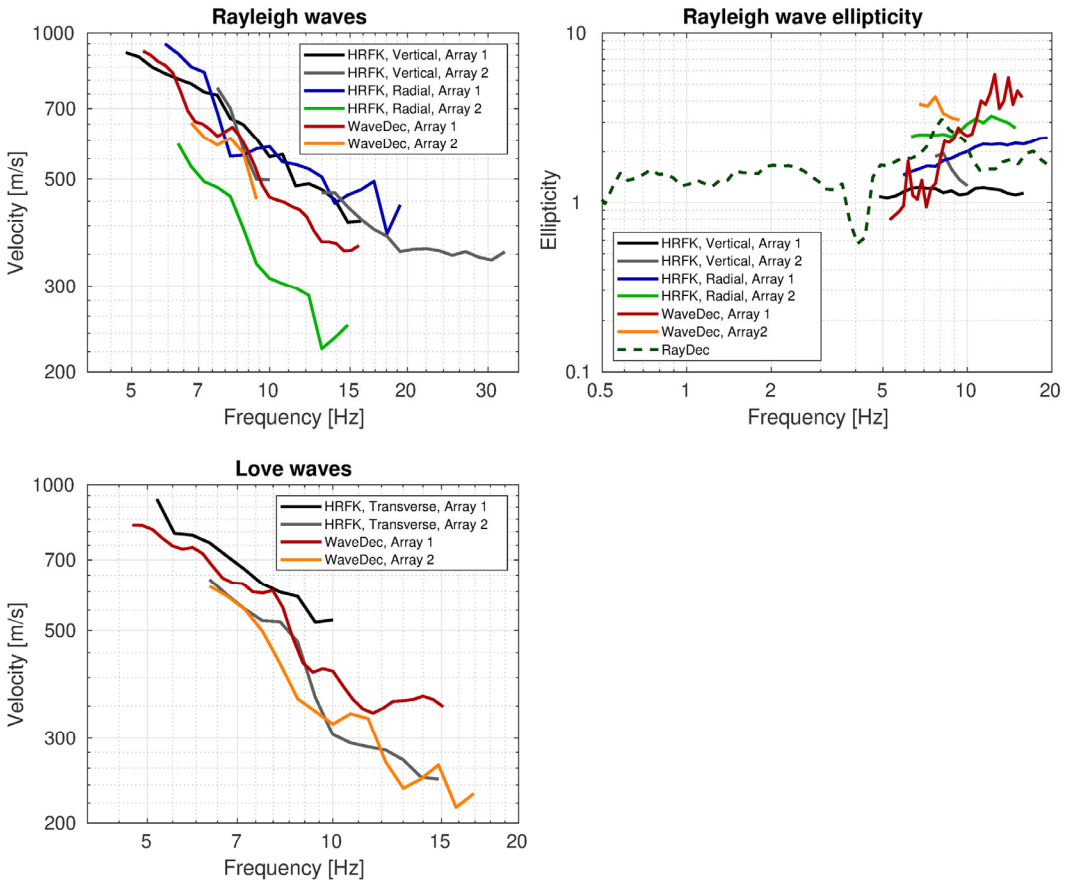

Figure 17 – Comparison of the estimated Rayleigh and Love wave phase velocity curves and the Rayleigh wave ellipticity curves from different processing methods for both arrays. The shown RayDec ellipticity curve corresponds to the station closest to the location of SCHK.

5.2 Active data processing

5.2.1 P-wave refraction

Seismic traces generated by different shots, with the seismic source at the same location (10 shots for each configuration), were summed – or stacked – in time domain. This was done to enhance the coherent seismic events generated by the controlled seismic source, and at the same time to minimize the incoherent noise present in the recordings (Foti et al., 2015). "Stacked" seismic sections, with greater signal-to-noise ratio, were hence obtained.

P-wave first-break arrival times were manually picked on the stacked seismograms for the vertical component from sources 1 (in the north) and 4 (in the south), the shot positions closest to the geophone array (Figure 3); the obtained travel-time curves are displayed in Figure 18. The two hodocrones are asymmetric, and show the typical appearance related to a sloping upper surface of the refractor (Reynolds, 2011). The curves were interpreted accordingly with the intercept time method (Reynolds, 2011). The obtained V_P model includes a superficial layer with V_P = 371 m/s, overlying a faster half-space with P-wave velocity of 816 m/s. The boundary between the two formations is slightly inclined, located at a depth of 3 m below src1, increasing to 4.3 m below src4.

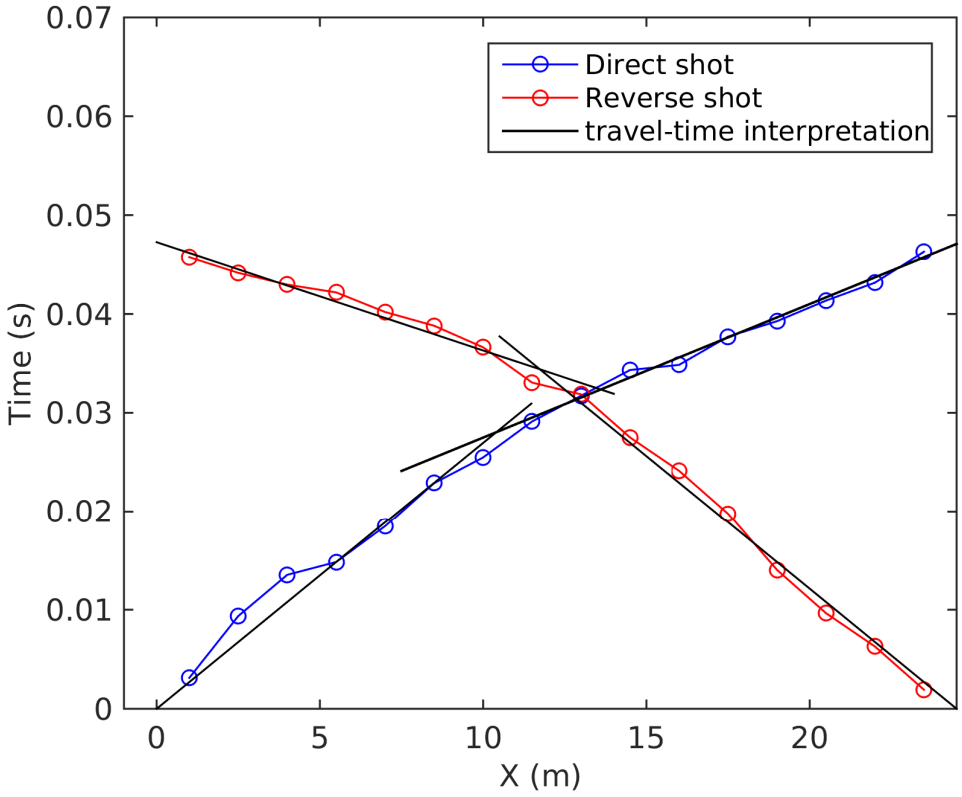

Figure 18 – P-wave refraction processing. P-wave travel-time hodocrones from src1 (direct shot, blue circles) and src4 (reverse shot, red circles). Black lines refer to the travel-time interpretation according to intercept time method. The X coordinate refers to the linear distance from src1.

5.2.2 MASW f-k processing

Rayleigh wave dispersion data were extracted from the vertical and longitudinal component seismograms from the recordings with source positioned in src3 and src6 (shooting points furthest from the geophone line, to avoid near-field effects; Foti et al., 2015). The considered seismic sections were processed by means of a 2D *f-k* (frequency-wavenumber) transform (Socco and Strobbia, 2004), in order to obtain a conversion of the recorded sets of traces from time-offset to frequency-wavenumber domain. *f-k* panels from single shot records with the same source and receiver positions were summed to obtain spectral images with greater S/N ratio.

The energy maxima corresponding to the Rayleigh wave dispersion curves were picked on these stacked *f-k* panels (Socco and Strobbia 2004, Foti et al., 2015). Spectral amplitude peaks from individual shot recordings were identified as well, and used to define the uncertainty intervals in the estimation of phase velocities (Socco et al., 2009; Boiero and Socco, 2010).

Figure 19 (left) shows the stacked *f-k* panels for sources at src3 and src6, vertical and longitudinal components, as well as the corresponding picked energy maxima. The obtained four Rayleigh wave dispersion curves show good mutual agreement, suggesting the absence of marked lateral variations below the geophone spread. Hence, these four curves were merged into a single, final dispersion curve (in blue in Figure 19, right inset), which appears to include a continuous branch extending

across the whole 10 – 80 Hz frequency band, with phase velocities decreasing from 500 to 200 m/s. This segment, being the slowest, is interpreted as the fundamental mode. Above the fundamental, a set of higher mode branches can be identified, most of them in the high frequency range (> 30 Hz), and just one at lower frequency (15 – 30 Hz). These segments cannot be attributed with certainty to any particular mode of Rayleigh wave propagation; an attempt to determine their mode numbering is shown in section 5.1.

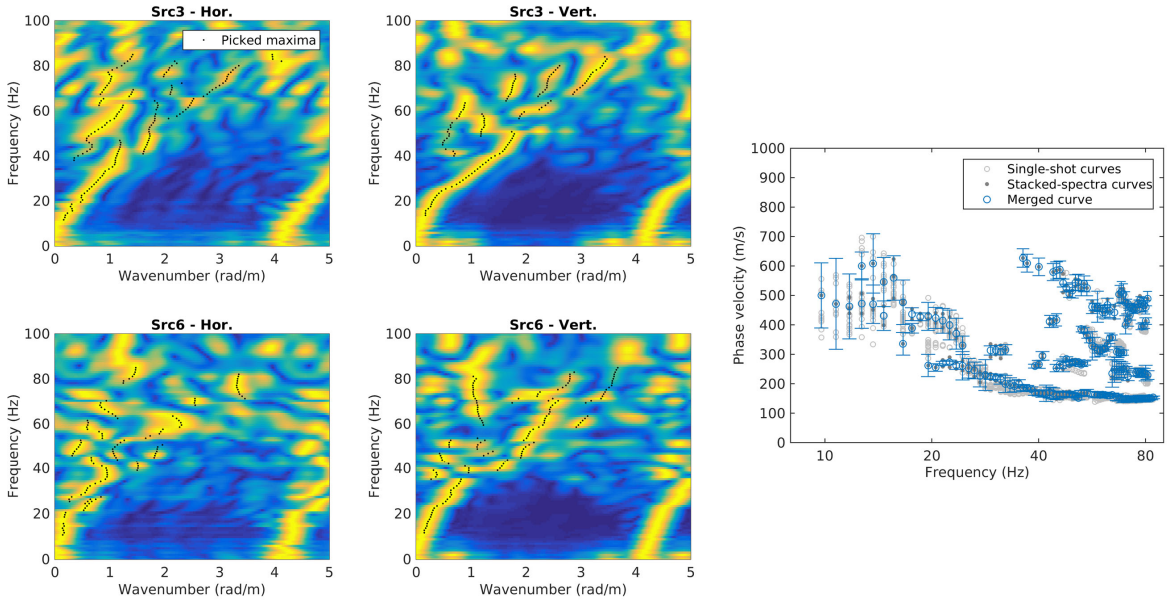

Figure 19 – MASW data fk processing. Left: stacked, normalized f-k spectra obtained from vertical and longitudinal components of seismic sections acquired with the source positioned in src3 or src6. Black dots are the picked energy maxima, corresponding to Rayleigh wave dispersion curves. Right: dispersion curve obtained by merging the curves from the four stacked fk spectra (src3 and 6, horizontal and vertical component); uncertainty intervals are provided by the standard deviation computed over the single-shot curves.

5.2.3 Wave field decomposition for active data

Three-component seismic traces acquired with the source positioned in src2 and src5 (Figure 3) were also processed with the WaveDecActive code (Maranò et al., 2017), with the aim of retrieving the properties of Rayleigh wave propagation in terms of both phase velocity and ellipticity. WaveDecActive implements a maximum likelihood algorithm for the analysis of Rayleigh waves generated by a controlled source. Differently from the conventional *f-k* analysis approach (see previous section), it is able to characterize the Rayleigh wave propagation both in terms of phase velocity and ellipticity angle. Another advantage on established MASW processing techniques is that WaveDec is properly modelling Rayleigh wave propagation also at short offsets (circular wavefront, near-field effects); therefore, we could resort to the seismic traces acquired with sources at src5 and src2 (Figure 3), closer to the geophone line than src6 and src3 and hence providing better S/N ratio. Figure 20 shows the obtained phase velocity estimates and their corresponding ellipticity angle values.

As already observed for the MASW *f-k* processing results, the curves obtained from direct and reverse shooting follow a similar trend (compare circles with crosses in Figure 20); this suggests the absence of sharp spatial variations at the receiver spread. Furthermore, the dispersion branches in Figure 17 show good agreement with the results of the MASW *f-k* analysis; in particular, the segment with slowest velocities is characterized by negative values of ellipticity angle (i.e. retrograde motion), as expected for the fundamental mode of Rayleigh waves in the absence of strong velocity contrasts in the subsoil.

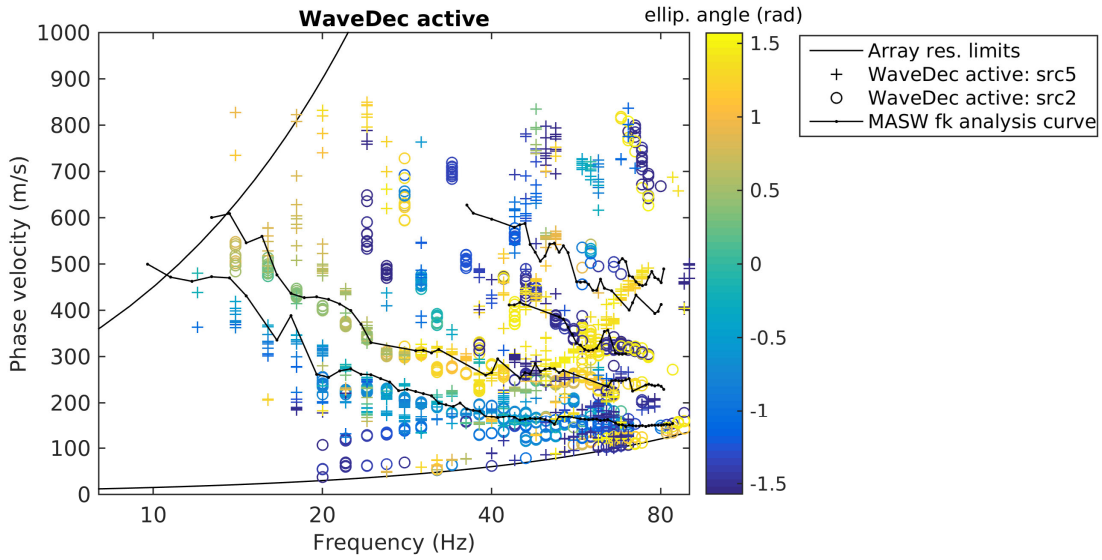

Figure 20 – WaveDec Active processing results. Rayleigh wave phase velocity estimates obtained from shots at src5 are represented as crosses; phase velocities from src2 as circles. For both, the color indicates the corresponding ellipticity angle. The array resolution limits (black lines) are comprised between wavelengths as long as twice the active array length (45 m, upper limit) and by wavelengths as short as the inter-geophone distance (1.5 m, lower limit).

6 Surface wave data inversion

The retrieved phase velocity dispersion curves of Rayleigh and Love waves as well as the Rayleigh wave ellipticity curve (section 5), were inverted for a 1D profile of the seismic properties of the subsurface. The adopted inversion strategy is the improved neighborhood algorithm (Wathelet, 2008), as implemented in the inversion software *dinver* of the Geopsy package (www.geopsy.org).

6.1 Mode numbering for Rayleigh wave dispersion curve

As shown in section 5, the univocal identification of the mode number for the extracted Rayleigh wave dispersion curve is possible only for the fundamental mode (see subsections 5.1.4, 5.1.5, 5.2.2, 5.2.3). For the tentative attribution of the other branches (particularly for the dispersion curve from active data), we followed an approach inspired by the procedures proposed by Maraschini and

Foti (2010) and Abdel Moati et al. (2013), and already implemented for the site characterization of station SBIK (see extensive description in Bergamo et al., 2018).

The basic idea is to test the agreement between the experimental apparent dispersion curve and a set of synthetic curves corresponding to a vast population of possible subsurface models, assuming a priori only the reliable modal attribution of few data points, and letting the others free to be assigned to the closest (in terms of phase velocity) simulated mode. The synthetic curve that best "explains" (i.e. closely matches) all (or most of) the experimental data points, and therefore achieves the lowest misfit, is assumed to propose the most likely modal attribution.

For this test, we considered as experimental data (Figure 21, left)

- The Rayleigh and Love wave dispersion curves from passive data, from either HRFK or WaveDec. We took into account only the curves from array 1. In fact, as array 2 was installed on the slope departing from the small plateau where array 1 and station SCHK are located, the subsurface "seen" by array 1 and 2 might not be the exactly the same. Data points from these curves were not attributed a priori to any particular mode, to allow for the possible "mode jumping" of energy at low frequency (Maraschini and Foti., 2010)
- The Rayleigh wave dispersion curve from active data, obtained from *fk* processing. Only the slowest branch was assigned a priori to the fundamental mode.

We tested a set of 1.75 million couples of Rayleigh and Love synthetic curves, with modes from fundamental to 5th higher for Rayleigh waves, and fundamental to 1st higher for Love waves. Each couple of curves stems from a randomly generated velocity model. The subsurface was parameterized as a stack of 7 layers overlying a half-space; wide boundaries were allowed for the random selection of V_S, V_P and thickness values. In fact, the purpose of this process is not inverting for a precise subsurface model, but rather to identify the modal attribution that best explains the experimental data of uncertain mode numbering.

The 20 best performing couples of synthetic Rayleigh and Love dispersion curves are shown in Figure 21, left panel. All simulated fundamental modes (Rayleigh and Love) consistently follow the identified experimental fundamental mode and the dispersion branches from passive data. For Rayleigh waves, a first (12 – 80 Hz) and second (40 – 80 Hz) higher mode are also consistently defined.

For completeness, we display in Figure 21 (right) the S-wave velocity models corresponding to the 20 best fitting sets of curves. We remark that these profiles do not represent the goal of the described procedure (which is identifying the optimal Rayleigh and Love wave mode numbering instead) and do not represent the inversion result for SCHK (which is illustrated in the next sections).

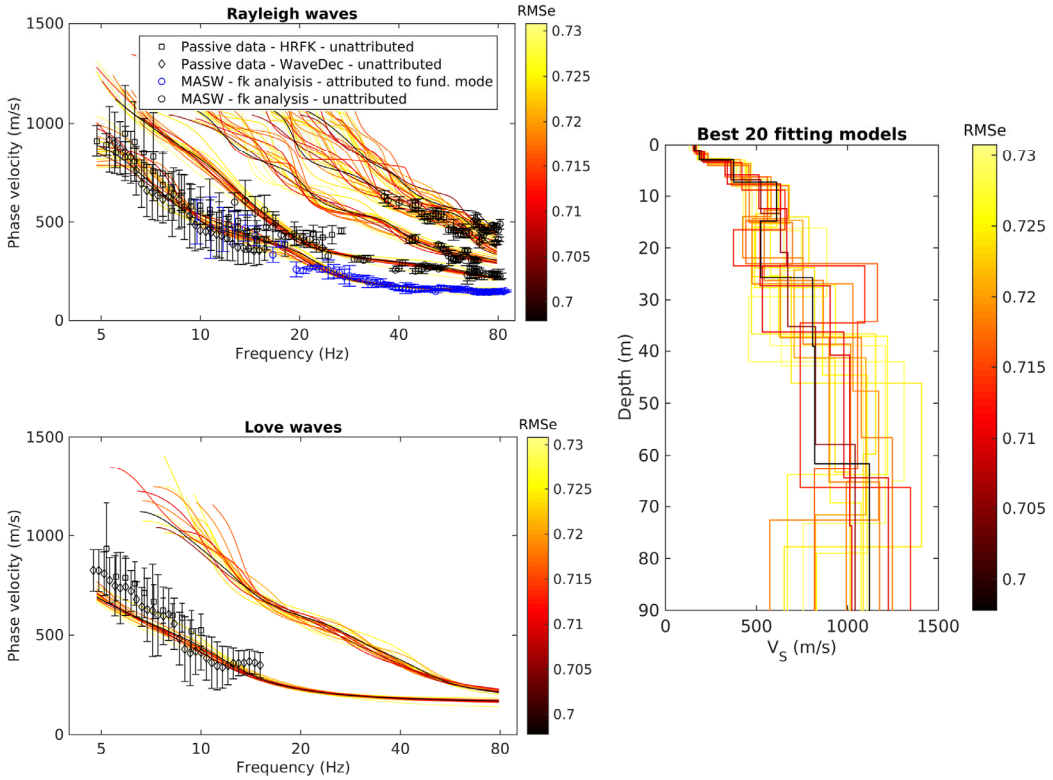

Figure 21 – Data-driven modal attribution. Left: data fit between the 20 best performing (lowest misfit) couples of synthetic multimodal Rayleigh and Love dispersion curves and the experimental curves from array 1 and the geophone line. Data points attributed a priori to the fundamental mode are in blue; all other data points were left free to be assigned to the closest simulated mode. Right: corresponding Vs profiles.

6.2 Inversion target

As earlier anticipated, we considered for the inversion the experimental curves stemming from array 1 passive recordings and the active data from the geophone array. The data of array 2 were discarded because of its distance and difference in altitude with respect to station SCHK. For both array 1 and active data, we preferred the curves obtained with the WaveDec code (sections 5.1.5, 5.2.3) as this provides a univocal couple of phase velocity and ellipticity curves, based on the joint analysis of both components of Rayleigh wave propagation (differently from *f-k* analysis)

The chosen ellipticity and phase velocity curves were re-sampled logarithmically, in compliance with the requirements of the inversion code *dinver* (www.geopsy.org).

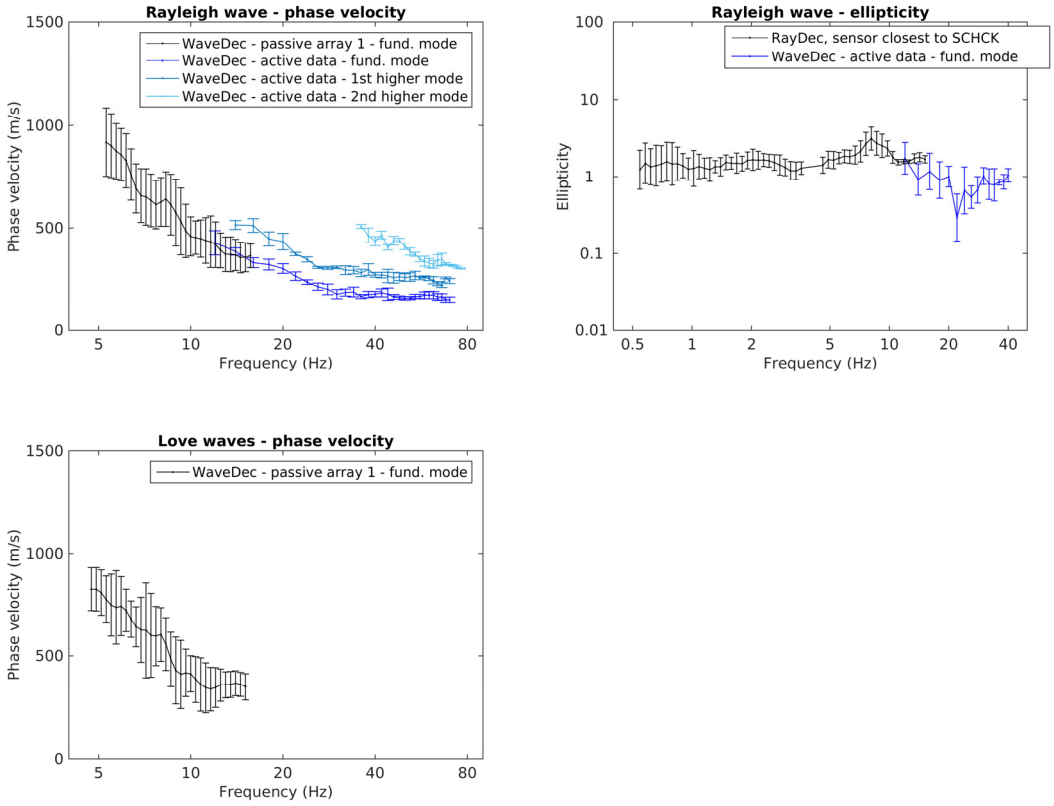

Figure 22 – Inversion target. Rayleigh wave (top left) fundamental and 1st-2rd higher modes from active and passive surface wave surveys, and Love wave (bottom left) fundamental mode exclusively from passive array data processing. Top right: fundamental mode ellipticity curves.

6.3 Parameterization of the model space

After several preliminary attempts, we adopted three different subsurface parameterizations:

1) In the first parameterization, the subsurface was modeled as a stack of 7 homogeneous layers, whose velocity (V_P, V_S) and thickness values were left free to vary within pre-defined ranges.
2) In the second parameterization, the subsurface was modeled as a stack of 8 homogeneous layers, whose velocity (V_P, V_S) and thickness values were left free to vary within pre-defined ranges.
3) In the third parameterization, the subsurface was modeled as a stack of 11 homogeneous layers with fixed thicknesses (increasing with depth), and whose velocity (V_P, V_S) values were left free to vary within pre-defined intervals.

In all parameterizations, density values are attributed a-priori to the layers: values increase with depth and they range from 1800 kg/m^3 (shallowest layer) to 2300 kg/m^3 (half-space). In all parameterizations, the velocity and thickness ranges for the three surficial layers (depths < 6 m) were derived from the surficial V_P model from P-wave refraction (section 5.2.1). The Poisson's ratios for these shallow layers was assigned as variable within 0.25 – 0.4 (values compatible with unsaturated soil material); below, the range was extended to 0.49, to allow for the presence of water-saturated material. As for the half-space, its Poisson's ratio interval was 0.2 – 0.3.

For the upper part of the subsurface model (below about 40 m), the velocities were forced to increase with depth for all parameterizations,; this constraint was waived for the lower part (with the exception of the half-space), as preliminary inversion attempts indicated an area of low velocity at these depths.

6.4 Inversion results

As anticipated, the code *dinver* from the Geopsy suite (ww.geopsy.org) was used as inversion software, implementing a search based on an improved neighborhood algorithm (Wathelet, 2008). Adopting the three different parameterizations presented in the previous section, we ran a total of 21 inversion runs (7 runs per parameterization); for each inversion run, we tested 200000 models in total, 100000 in the first random search phase and 100000 more in the successive refinement phase. In Figures 23-26 we compare the results obtained from three sample inversion runs, each following a different parameterization (7, 8 or 11 layers). The minimum achieved RMSEs are quite similar (0.838, 0.822 and 0.845, respectively), and so is the misfit between experimental and simulated curves (Figures 23-25). The data fit is generally good; the more remarkable disagreements are met in the ellipticity curve (upper right inset in Figures 23-25). Whichever the parameterization, simulated curves draw a "hump" at around 15 Hz, which is absent from the experimental data. Furthermore, simulated ellipticities do not follow the low-frequency peak at 0.7 Hz in the experimental curve. The reason is that the adopted parameterizations, as well as the phase velocity data, do not allow reaching the depth to which this low-frequency feature is related. It was not possible to fit it in the inversion process, as this would have meant increasing significantly the number of layers (i.e. the number of unknowns), without phase velocity data to somehow constrain their velocity properties.

As for the V_S profiles, we obtained similar models from all parameterizations (Figure 26). The shallow 3 m exhibit very low velocities (160 – 200 m/s); below, in the depth range from 3 to 23 m, a layer with much higher V_S is found (500 – 600 m/s). The S-wave velocity increases further to 900-1200 m/s down to approx.. 45 m of depth; below, a low-velocity layer is present (500-850 m/s), whose lower interface reaches about 75 m of depth and rests on the half-space (with V_S of 1400 – 1800 m/s). The models achieving the minimum misfit from each individual inversion run (21 in total, $0.822 < RMSE < 0.910$) were collected and they constitute the final result of the inversion process (Figure 27).

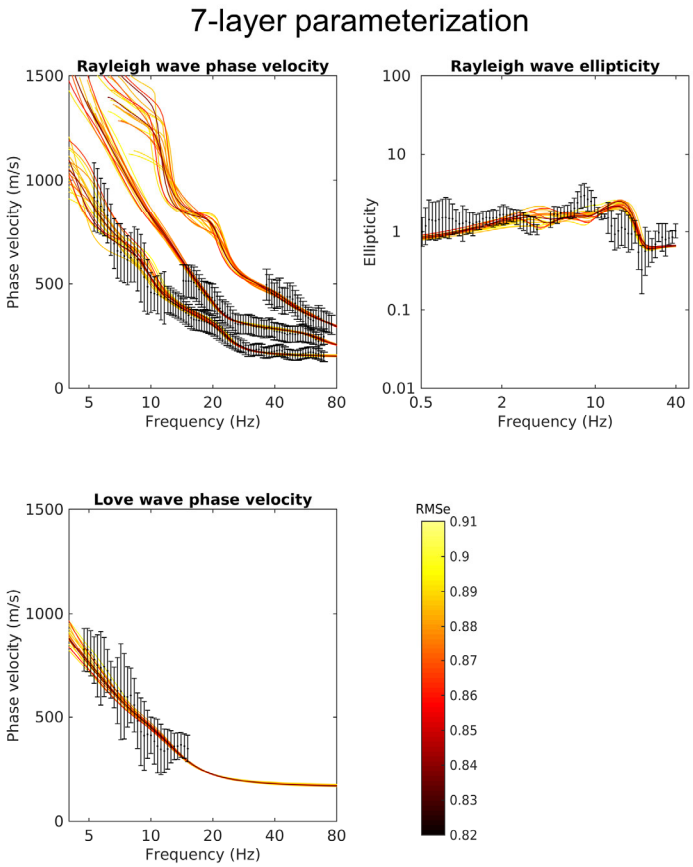

Figure 23 – 7-layer parameterization, sample inversion run: fit between experimental data (black dots with error bars) and synthetic curves (colored lines) for the 20 best performing models.

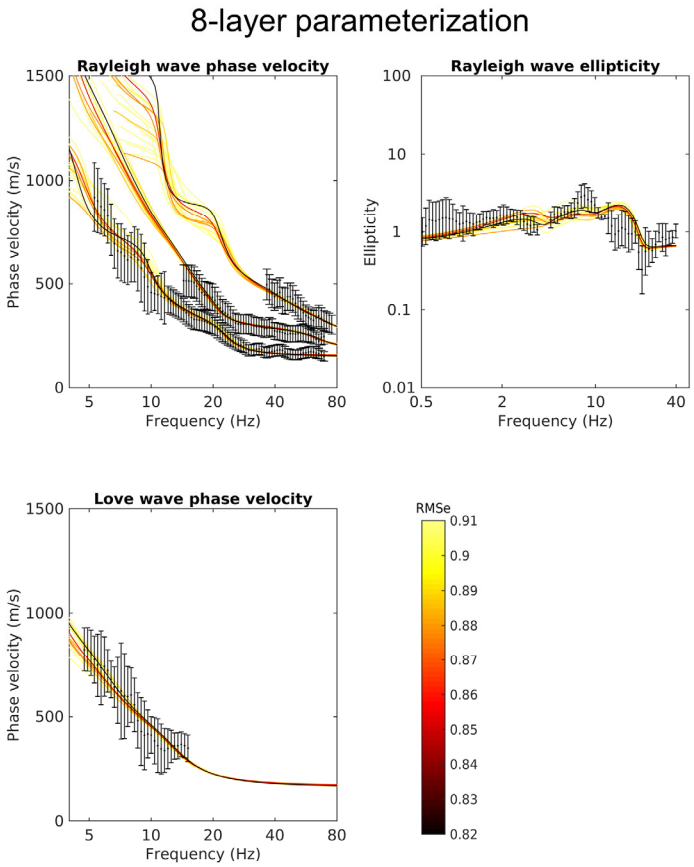

Figure 24 – 8-layer parameterization, sample inversion run: fit between experimental data (black dots with error bars) and synthetic curves (colored lines) for the 20 best performing models.

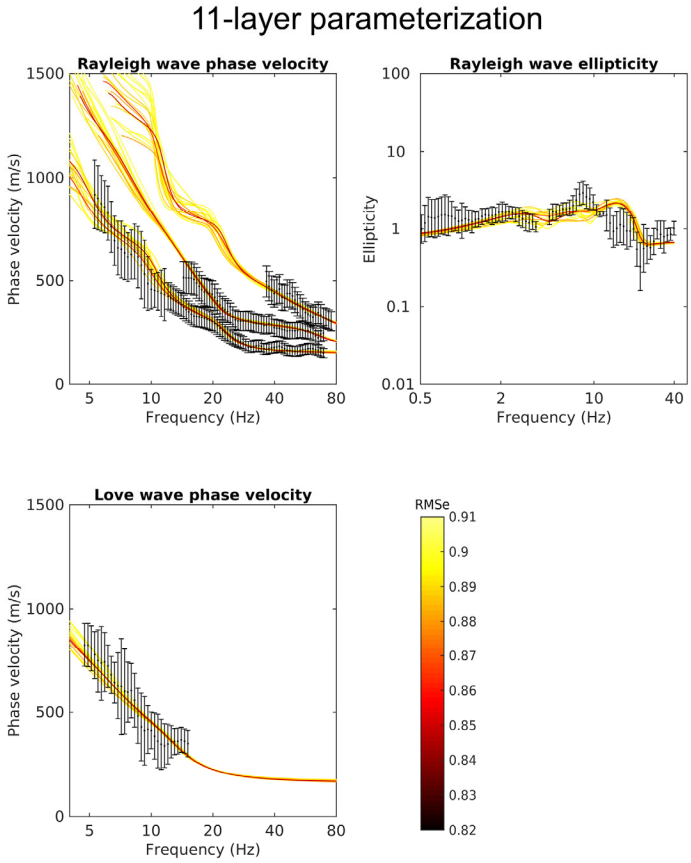

Figure 25 – 11-layer parameterization, sample inversion run: fit between experimental data (black dots with error bars) and synthetic curves (colored lines) for the 20 best performing models.

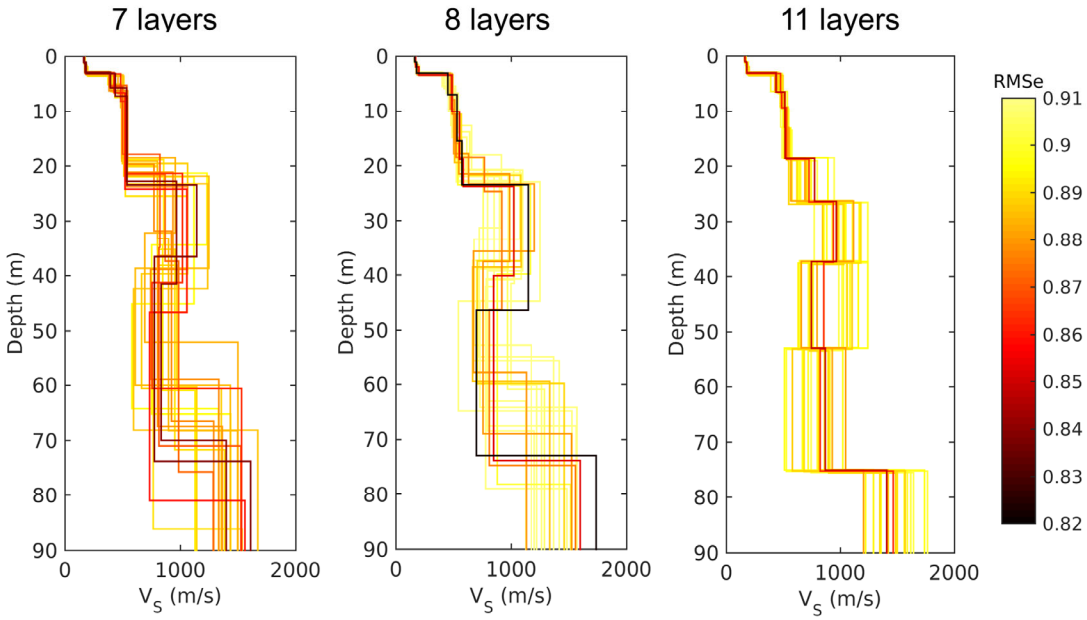

Figure 26 – Vs profiles of the 20 best-fitting subsoil models obtained from three inversion runs, each adopting a different subsurface parameterization.

7 Interpretation

In this section, the geological interpretation of the obtained velocity profiles (Figure 27) is discussed.

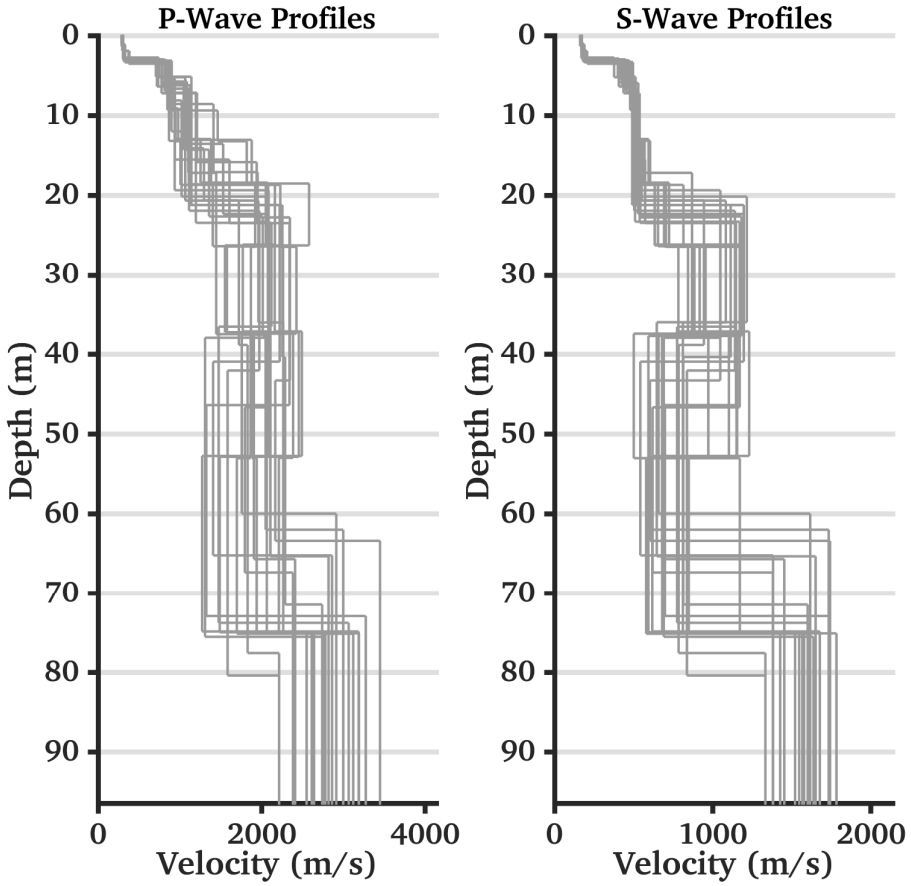

Figure 27 – Set of 21 best performing velocity models, each obtained from a different inversion run adopting either the 7-, 8-, or 11-layer subsurface parameterization.

7.1 Interpretation of the velocity profiles

The final result of the inversion process is constituted by a set of 21 V_S-V_P velocity models, each obtained from a different inversion run adopting either the 7-, 8-, or 11-layer subsurface parameterization (7 runs per parameterization); these velocity models are represented in Figure 27, where they show a good reciprocal consistency. The surficial soil cover is ~3 m thick and it appears to be quite soft (V_S = 160 – 200 m/s). Below, the subsurface can be simplified as a 3-layer over half-space structure, alternating softer (3 – 22 m and 45 – 75 m depth) with stiffer (22 – 45 m, > 75 m depth) materials. Considering the local geology and the morphology of the Rabiusa valley at Churwalden (Figure 1), it is possible to ascribe this constitution to a fluvial terrace structure. In other words, the quaternary cover of the valley should be constituted mainly by a succession of fluvial terraces, having different stiffness as they have been created at different ages and are

constituted by different materials. This hypothesis seems to be confirmed by the agreement between the retrieved S-wave velocity models and the topographical profile of the valley (Figure 28). In fact, the interfaces in the V_S profiles are found at approximately the same depths as sharp changes in the topographical slope. Therefore, the upper layer of this terraced structure (3-22 m depth) appears to be relatively soft (V_S = 500 – 600 m/s), probably constituted by incoherent gravel. Below (22-45 m), the material appears to be stiffer (V_S = 800 – 1200 m/s), and it is possibly constituted by river gravel which underwent a cementation process. The different level of cohesion between these two formations is also evident in the angle of their topographical slope, much steeper for the 22 – 45 m layer. Correlating this stratigraphic information with the appearance of the H/V curves (section 5.1.1), it is possible to associate the V_S interface at ~22 m with the H/V f_1 peak at 8 – 20 Hz (Figures 7, 8, 9). As this peak appears to move to higher frequencies as one proceeds further from the cliff where SCHK is located (Figure 9), we can speculate that the V_S discontinuity at 24 m depth actually corresponds to a sloping interface, inclined towards the valley centre.

Below the stiff formation within 22 – 45 m depth, we find a softer layer (V_S = 600 – 800 m/s), possibly constituted by incoherent river gravel deposits. Its lower boundary is estimated to be located at around 75 m depth, where the S-wave velocity increases to 1400 – 1800 m/s (probably the weathered slate outcropping to the right side of the river bed, Figure 28).

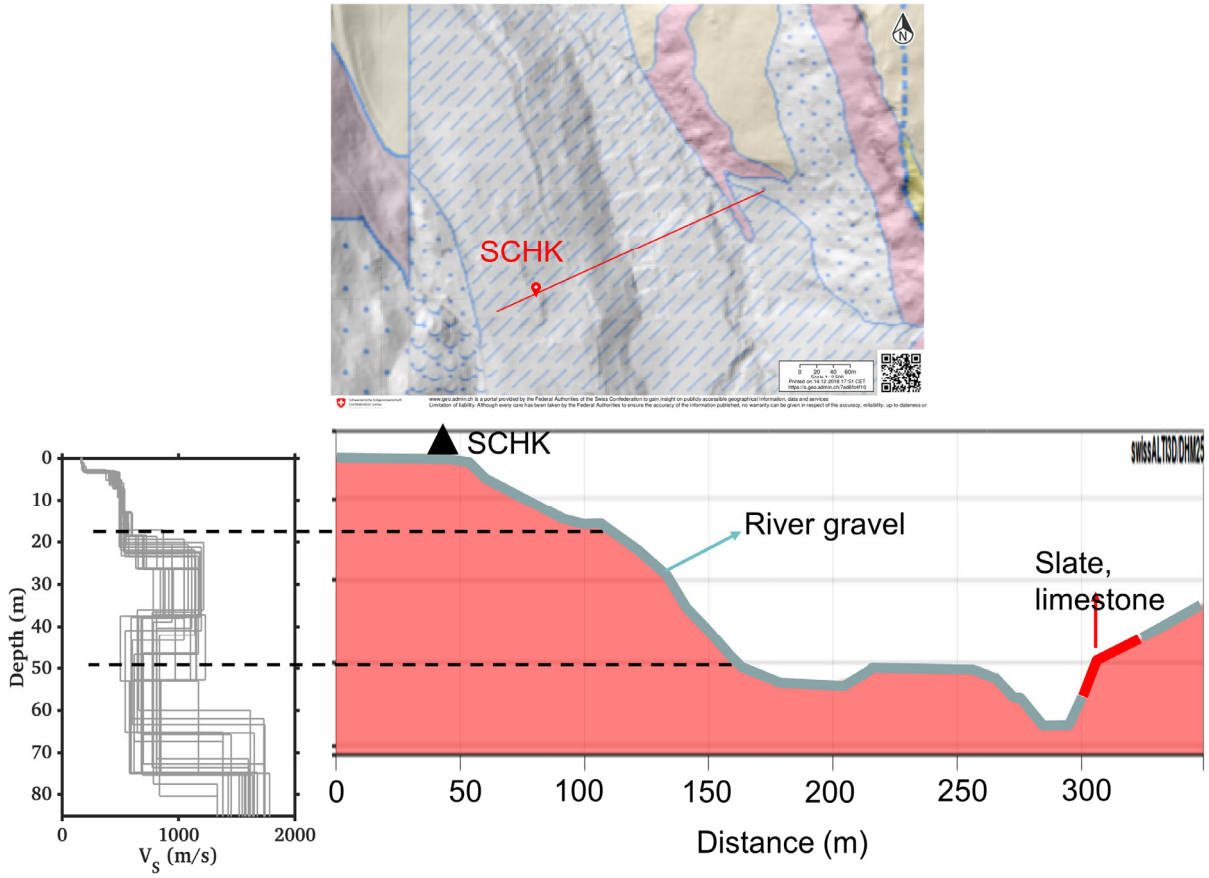

Figure 28 – Topographic profile (bottom centre) of a section spanning the left valley flank down to the valley bed at the location of SCHK (upper panel; © 2018 Swisstopo, JD100042). The best performing V_S profiles (same as in Figure 27) are represented in the left bottom panel, for comparison with the topographical section.

6.1 Quarter-wavelength representation

In Figure 29, we show the quarter-wavelength representation (Joyner et al., 1981; Poggi et al., 2012) in terms of depth (top panel), velocity (centre) and impedance contrast (bottom), averaged over the selected final profiles of Figure 27.

The quarter-wavelength velocity at the frequency of the quarter-wavelength depth of 30 m corresponds to a V_{S30} value of 479 m/s.

The quarter-wavelength impedance contrast (bottom panel) shows three peaks at 2.5, 6.5 and 15 Hz; they correspond, respectively, to the interfaces at approx. 75, 22 and 3 m depth in the estimated subsurface models (Figure 27).

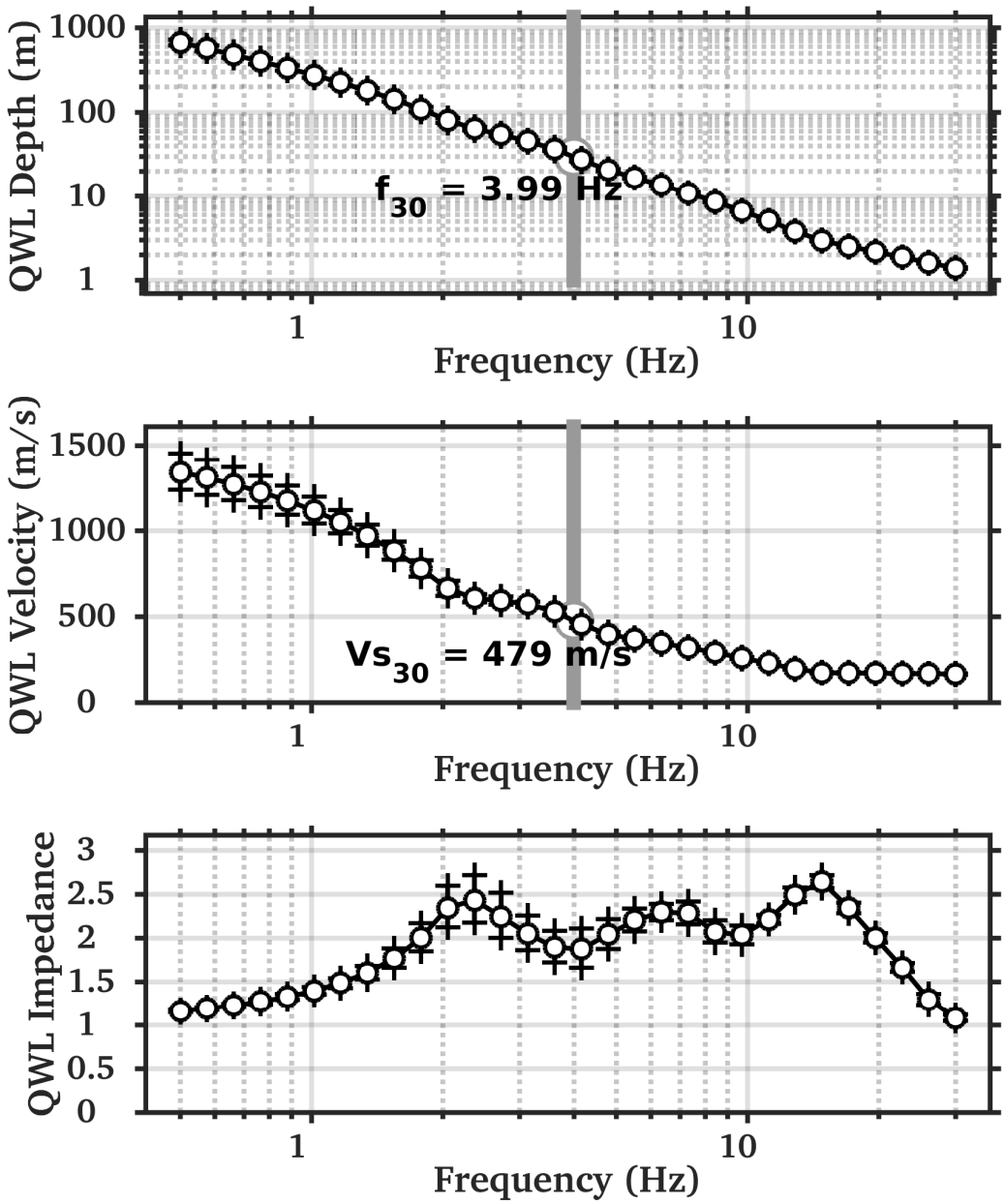

Figure 29 – Average quarter-wavelength (qwl) representations for the final profiles displayed in Figure 19. Top: qwl-depth; center: qwl-velocity; bottom: qwl-impedance contrast. The gray line in the top and center panel refers to Vs_{30}.

6.2 SH transfer function

The theoretical SH-wave transfer functions for vertical propagation (Roesset, 1970) were computed for the selected models (profiles in Figure 27), and corrected for the Swiss reference rock model (Poggi et al., 2011).

In Figure 30, the average of these functions (blue line), is compared with the amplification function obtained by empirical spectral modeling (red line; Edwards et al., 2013) and referred to the Swiss reference rock. Both the simulated and the empirical transfer functions agree in identifying a first peak at around 2.5 Hz, which is to be related to the interface between river gravel deposits and weathered rock estimated to be at around 75 m depth (Figure 27).
Above the fundamental peak at 2.5 Hz, the empirical amplification function shows a second peak at 8.9 Hz, which is found at a somewhat lower frequency (6.9 Hz) in the synthetic functions; this peak corresponds to the velocity contrast at 22 m depth (Figure 24).

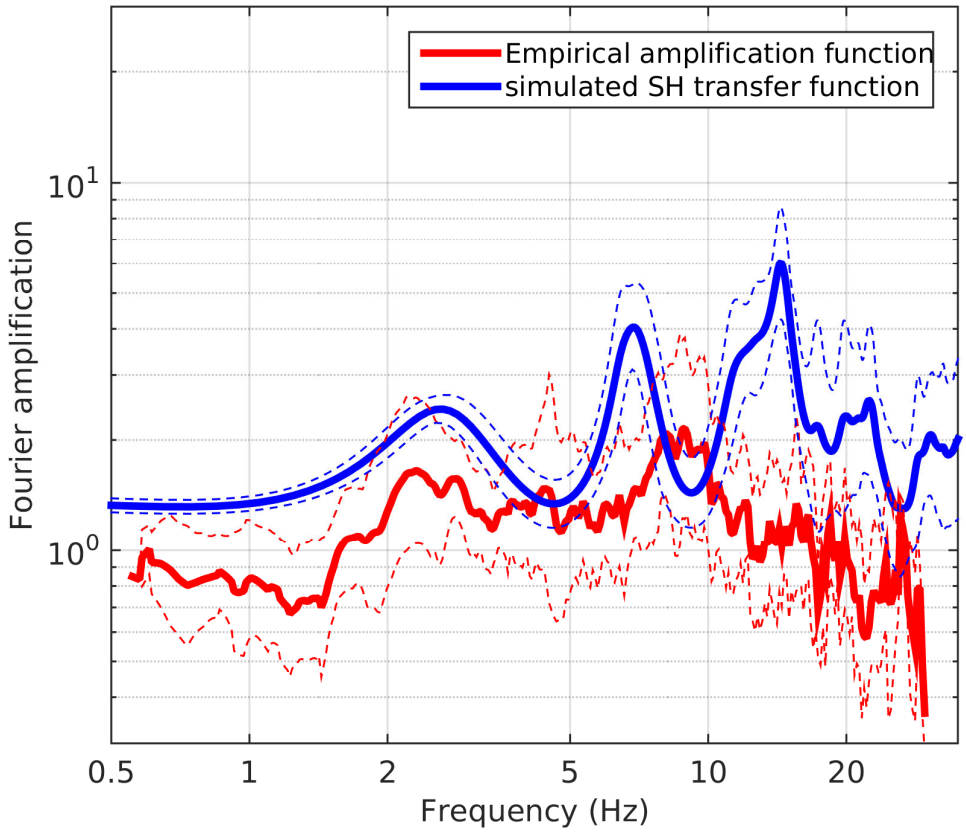

Figure 30 – Average of the modeled SH transfer functions (blues line) from the selected velocity profiles (Figure 27), corrected for the Swiss reference rock model. In red, the empirical amplification function obtained from spectral modeling.

8 Conclusions

Active and passive seismic surveys were performed to characterize the structure of the subsurface below the SSMNet station SCHK, located in the village of Churwalden (GR), at the edge of a terrace on the left flank of the Churwaldnertal. Passive data were processed to derive Rayleigh and Love wave phase velocity dispersion curves, and a Rayleigh wave ellipticity curve; active data were analyzed to estimate the high-frequency portion of the Rayleigh wave phase velocity and ellipticity curves, and to obtain a V_P model for the shallow subsoil from P-wave refraction.

The analysis of single-station noise recordings via H/V analysis allowed identifying the fundamental frequency of the site as 0.75 Hz; at higher frequencies, a second peak is present, increasing from 8 Hz (at the edge of the terrace, where SCHK is located) to 15 – 20 Hz (where the terrace joins the mountain flank).
The analysis of single-station noise recordings via polarization analysis did not indicate 2D or 3D resonance phenomena; preferential directions of propagation have been identified at very low frequency (0.2 – 0.5 Hz, along a south-west to north east axis) and at higher frequencies (5 – 20 Hz, along a north-west – south-east direction, i.e. the main axis of the valley).
The subsurface structure at SCHK is quite complex. The surficial soil cover is about 3 m thick and it appears to be quite soft (V_S = 160 – 200 m/s). Below, the subsoil can be simplified as a 3-layer over half-space model, alternating softer materials (probably unconsolidated gravel deposits, at 3 – 22 and 45 – 75 m depth, with V_S 500 – 850 m/s) with stiffer formations (22 – 45 m depth, V_S 900 – 1200 m/s, probably cemented gravel; and > 75 m depth, $V_S \approx$ 1400 – 1800 m/s, possibly weathered rock). Considering the local geology and the morphology of the Rabiusa valley at Churwalden, it is possible to ascribe this structure to a succession of fluvial terraces with varying levels of cementation. The interface between the shallowest and the second terrace formations (~22 m depth), with V_S sharply increasing from approx. 500 to ~1100 m/s, determines the f_1 peak from H/V curves at 8 Hz at the location of SCHK. The fundamental frequency f_0 (0.75 Hz) is not associated to any feature of the reconstructed subsurface model (covering a maximum depth of approximately 90 m); rather, it could be ascribed to a much deeper soft-to-stiff rock interface.
The 1D transfer function derived from the reconstructed S-wave velocity model manages to reproduce quite well the fundamental peak at 2.5 Hz in the empirical amplification function, which corresponds to the ~75 m deep interface between gravel deposits and weathered rock below.
The obtained V_{S30} is 479 m/s; H_{800} (depth where V_S exceeds 800 m/s) is 23.2 m; therefore, the site can be classified as type B according to Eurocode 8 (CEN, 2004), and as type C following SIA261 (SIA, 2014).

References

Abdel Moati, W.H., D. Boiero, and L.V. Socco, 2013. A tool for fast underground characterization for trenchless pipeline construction by horizontal directional drilling technology. 11th Offshore Mediterranean Conference and Exhibition, Ravenna, Italy, March 20-22 2013.

Bard, P.-Y., and M. Bouchon, 1985. The two-dimensional resonance of sediment-filled valleys, Bull. Seismol. Soc. Am. 75, no. 2, 519–541.

Bergamo, P., M. Hobiger and D. Fäh, 2018. Site characterization report – SBIK Biel/Bienne (BE), Kongresshaus/Palais des Congrès. SED report.

Bergmann, U., Die ehemalige Prämonstratenser Klosterkirche St. Maria und Michael Churwalden, Schweizerische Kunstführer GSK, 1997.

Boiero, D., and L. V. Socco, 2010, Retrieving lateral variations from surface wave dispersion curves analysis: Geophysical Prospecting, **58**, 977–996

Burjanek, J., J.R. Moore, F.X. Yugsi Molina, and Donat Fäh, 2012. Instrumental evidence of normal mode rock slope vibration. GJI, 188, 559-569.

CEN, 2004. Eurocode 8: Design of structures for earthquake resistance – Part 1: general rules, seismic actions and rules for buildings. European Committee for Standardization, en 1998-1 edition.

Edwards, B., Michel, C., Poggi, V., and Fäh, D. , 2013. Determination of Site Amplification from Regional Seismicity : Application to the Swiss National Seismic Networks. Seismological Research Letters, 84(4).

Fäh, D., F. Kind, and D. Giardini, 2001. A theoretical investigation of average H/V ratios. GJI, 145, no. 2, 535-549.

Foti, S., Lai C.G., Rix G.J., and C. Strobbia, 2015, Surface Wave Methods for Near-Surface Site Characterization: CRC Press, Taylor & Francis Group LLC

Hobiger, M., P.-Y. Bard, C. Cornou, and N. Le Bihan, 2009. Single station determination of Rayleigh wave ellipticity by using the random decrement technique (Raydec). GRL, 36, L14303

Joyner, W. B., Warrick, R. E., and Fumal, T. E., 1981. The effect of Quaternary alluvium on strong ground motion in the Coyote Lake, California, earthquake of 1979. Bulletin of the Seismological Society of America, 71(4):1333–1349.

Maranò, S., C. Reller, H.A. Loeliger, and D. Fäh, 2012. Seismic waves estimation and wavefield decomposition: application to ambient vibrations. GJI, 191, 175-188

Maranò, S., M. Hobiger, P. Bergamo and D. Fäh, 2017. Analysis of Rayleigh Waves with Circular Wavefront: a Maximum Likelihood Approach. GJI, 210 (3), 1570-1580.

Maraschini, M., and S. Foti, 2010. A Monte Carlo multimodal inversion of surface waves. GJI, 182 (3). 1557 – 1566.

Nakamura, Y., 1989. A Method for Dynamic Characteristics Estimation of Subsurface Using Microtremor on the Ground Surface. Quarterly Report of RTRI, vol. 30, no. 1, 25- 33.

Park, C. B., R. D. Miller, and J. Xia, 1999. Multichannel analysis of surface waves: Geophysics, **64**, 800–808.

Poggi, V., Edwards, B., and Fäh, D., 2011. Derivation of a Reference Shear-Wave Velocity Model from Empirical Site Amplification. Bulletin of the Seismological Society of America, 101(1):258–274.

Poggi, V., B. Edwards and D. Fäh, 2012. The quarter-wavelength average velocity: a review of some past and recent application developments. 15th WCEE, Lisbon 2012

Poggi, V., and D. Fäh, 2010. Estimating Rayleigh wave particle motion from three component array analysis of ambient vibrations. GJI, 180, no. 1, 251-267.

Redpath, B. B., 1973. Seismic refraction exploration for engineering site investigations: National Technical Information Service, Technical Report E-73-4.

Reynolds, J. M., 2011. An introduction to applied and Environmental Geophysics: John Wiley & Sons, Ltd.

Roesset, J., 1970. Fundamentals of soil amplification. In: Hansen, R. J., editor, Seismic Design for Nuclear Power Plants, pages 183–244. M.I.T. Press, Cambridge, Mass.

Schwarz-Zanetti, G., 2008. Das Churwaldner Erdbeben vom 3. September 1295. In: M. Gisler, D. Fäh, D. Giardini (editors), Nachbeben – Eine Geschichte der Erdbeben in der Schweiz, p. 35 – 40. Haupt Verlag, Bern.

SIA, 2014. SIA 261 Einwirkungen auf Tragwerke. Société Suisse des ingénieurs at des architectes, Zurich, Switzerland.

Socco, L.V., D. Boiero, S. Foti, and R. Wisen, 2009. Laterally constrained inversion of ground roll from seismic reflection records: Geophysics, **74**, no. 6, G35-G45.

Socco, L.V., and C. Strobbia, 2004. Surface-wave method for near-surface characterization: a tutorial: Near Surface Geophysics, **2**, no. 4, 165-185.

Swisstopo, 2018. 1:25000 Geological Atlas, nr. 1195 and 1196 (Reichenau and Arosa)

Wathelet, M., 2008. An improved neighborhood algorithm: Parameter conditions and dynamic scaling. GRL, 35, no.9, 1-5